High-frequency Fluctuation of Air Temperature during a Heatwave Event in Urban Environment and the Physical Mechanism Behind

Ruiqing Du, Chun-Ho Liu *, and Yixun Liu

Department of Mechanical Engineering, The University of Hong Kong, Hong Kong

Revised Manuscript No. BAE-D-23-02849

submitted

to

Building and Environment

on

August 26, 2023

**Correspondence:*

Chun-Ho LIU

Department of Mechanical Engineering,

7/F Haking Wong Building,

The University of Hong Kong,

Pokfulam Road, Hong Kong SAR, CHINA

Tel: +852 3917 7901 / + 852 9788 7951

Fax: +852 2858 5415

liuchunho@graduate.hku.hk

https://aplhk.tech

ORCID: 0000-0002-4609-524X

Abstract

Heatwaves threaten human health and power systems. Urban climate is non-stationary and wide-spectrum, with high-frequency temperature and wind-speed variations that could overload power grids and expose people to extreme heat. In this study, Hilbert-Huang transform (HHT) was unprecedentedly used to decompose the urban-scale temperature ($IMF\theta1$ to $IMF\theta6$) and wind-speed ($IMFW1$ to $IMFW6$) signals during a 5-day heatwave event into 6 intrinsic mode functions (IMFs). The spatio-temporal characteristics, physical mechanism, and effective ranges of high-frequency components (IMF1 to IMF4) were unveiled. Temperature (wind speed) $IMF\theta1$ to $IMF\theta4$ ($IMFW1$ to $IMFW4$) had a temporal scale of 2.63 hr (2.53 hr), 5.88 hr (5.78 hr), 13.16 hr (9.84 hr), and 22.72 hr (19.05 hr); as well as a spatial scale of 2.31 km (0.99 km), 4.29 km (1.65 km), 5.94 km (2.64 km), and 6.6 km (2.97 km), respectively. The physical mechanisms of IMF1 to IMF4 were composed of turbulence and heat storage/release; disturbance induced by mountainous terrain and slope flows; land/sea breeze, together with anthropogenic heat. Besides, the peaked amplitudes of $IMF\theta1$ were most risky in compact/open high-rise urban (1.4 °C to 1.6 °C) rather than rural (0.6 °C to 1.0 °C) areas. The foothill areas within 8-km coverage were susceptible to $IMF\theta2$ (1 °C to 2.1 °C). $IMF\theta3$ (0.6 °C to 3.6 °C) was effective in urban areas within 10 km from coastline. $IMF\theta4$ (2.5 °C to 3.5 °C) exhibited the most intense fluctuation in urban/suburban areas. The outcome provides references for policy makers to mitigate heat-related risks. (247 words)

Keywords: empirical mode decomposition (EMD); extreme temperature; heatwave; high-frequency fluctuation; Hilbert-Huang transform (HHT); intrinsic mode function (IMF); urban temperature

1. Introduction

Rapid urbanization induces global warming and more frequent temperature extremes. The unusual warmth has tremendous impacts on public health and power security. High temperature could result in life-threating thermal stress of human body by inhibiting heat loss and metabolic regulation [1]. As a remedial measure for space cooling, the usage of air-conditioning (AC) would surge. Previous studies have reported that space-cooling-related energy demand could be over 50% of the total in China [2] and the United States [3]. It could result in power shortage or even electric-grid failure [4]. For example, the 2022 heatwave event caused at least 26,000 mortalities in Europe. Moreover, the 2019 heat-related blackout led to 73,000 citizens being suffered in New York [5]. Therefore, unveiling the mechanism of peaked urban temperatures during heatwave events is essential to urban planning and energy policy.

Air-temperature fluctuation plays an important role in urban environment. The mortality and building energy consumption are sensitive to the fluctuating temperatures during extremely hot days. In Hong Kong (HK), for example, every 1 °C increase would induce 4.1% [6] and 9.2% [7] increases in fatality rate and building energy consumption, respectively, under extreme temperatures. Whereas, urban thermal environment is a multi-scale process governed by a range of factors including terrain, urban morphology, and construction materials, etc. Among others, some factors, such as solar radiation and synoptic weather conditions, could induce low-frequency temperature variations (temporal period ≥ 24 hr). On the other hand, atmospheric turbulence and local winds, could cause high-frequency temperature fluctuations (temporal period < 24 hr) [8]. Most of these changes are aperiodic and stochastic. Under this circumstance, acute temperature fluctuations are induced that tremendously soar (peaked) power demand.

During extreme heatwave events, power grids are already on the verge of collapse. In case of sudden, huge power demand, the electricity infrastructure would be overloaded that risks the cities to blackouts [1, 9]. Once a city is in blackout, the outage of AC system could cause increased indoor temperature. Moreover, these non-linear, non-stationary fluctuations could induce uncertainties and anomalies in urban microclimate. It would lead to harmful impact on public health and social activities. Urban planners might find it difficult to handle those unknown threats. Thus, it is necessary to extract the high-frequency components from the (time series of) urban temperatures and explore the physical implication behind.

In this study, the complicated, extreme temperature data in urban environment were decomposed. The associated high-frequency components and the corresponding physical processes were examined. To analyze the fluctuating temperatures, the techniques from the signal-processing sector have been commonly adopted. Numerous spectral decomposition approaches, such as Fourier decomposition [10, 11] and Wavelet transform [12], have been employed with predetermined functions and time scales. Whereas, urban climate is chaotic, non-linear, and non-stationary. As such, the local time scale is unknown in prior [13]. Lately, a method to analyze such complicated data was fostered in the Hilbert-Huang Transform (HHT) [14]. The key step of HHT is empirical mode decomposition (EMD) which is capable of separating any (original) signals into a finite set of orthogonal components called intrinsic mode functions (IMFs). Among others, EMD is entirely data-adaptive that automatically determines the time scales according to the intrinsic data properties, avoiding the a priori choice of time-scale functions [15]. EMD has been applied to the long-term (a few decades) data analyses of the urban temperatures in Mexico City [16], Shanghai [17], Chongqing [18], Taipei [19], Milan [20], Southern India [21], and the United States [15]. Besides, it has been employed to examine the impact of ambient temperatures on the power consumption in Sarajevo City [22] and the effect of vegetation on the air temperatures in Three Gorges Reservoir Region, China [23]. Moreover, it was used to analyze the pedestrian-level wind data in Sydney [24]. It was found that EMD could capture the amplitude-frequency fluctuations, especially the high-frequency temperature anomalies or local characteristic of winds. In addition, EMD combined with HHT that enabled the investigation of the multi-scale variability of extreme temperatures over a region.

High-resolution meteorological data are crucial to differentiate the inhomogeneous urban climate nowadays. Weather Research and Forecasting (WRF) model coupling the Building Effect Parameterization (BEP) and Building Energy Model (BEM) [25, 26] is a workaround to refine the spatio-temporal resolution of urban meteorological variables. As a multi-scale model, it enables the urban-climate simulation to consider the mesoscale boundary conditions, natural terrain, building properties, and urban configuration. WRF-BEP/BEM has been validated and applied extensively in studies of urban thermal environment especially heatwave events [27].

To the best knowledge of the authors, however, there are few studies employing EMD on urban temperature datasets from the WRF-BEP/BEM model. Moreover, the short-term, high-frequency (temporal period < 24 hr) components in urban temperatures during typical heatwave events and their physical explanation are rarely explored. Therefore, the pressing need for decomposing broad-spectrum, extreme temperature patterns into interpretable components arises. Such decomposition is helpful to mitigate urban heat island (UHI) and avoid disasters during extremely hot days. Urban planners could formulate the most cost-effective strategy according to the temperature variations in different spatio-temporal scales. Besides, the physical processes of individual components are essential to the understanding of the mechanism behind extreme temperatures and the related countermeasures. Unlike the traditional methods, such as Fourier decomposition and Wavelet transform, EMD is adaptive and requires no predefined temporal function so is more suitable for chaotic, non-stationary urban thermal processes. Thus, it is worthy to use EMD to characterize urban temperatures as well as reveal the implication of individual components.

To bridge the aforementioned knowledge gap, in this paper, we study various high-frequency, irregular components in (hourly) urban temperature during extremely hot days. First, the urban temperature during a typical heatwave event (June 23 to 27, 2016) in Hong Kong is calculated using the WRF-BEP/BEM model [28]. Afterward, EMD/HHT is employed to decompose the temperature signals into IMFs. The spatio-temporal properties and the physical mechanism of the IMFs are further diagnosed. Furthermore, the thermal impact of each high-frequency component of temperature fluctuation on urban environment and the effective range are assessed according to the peaked IMF amplitudes.

The specific objectives of this study are to: (1) present a scheme to decompose the temperatures during heatwave events into the mean and several high-frequency fluctuating components; (2) examine the spatio-temporal characteristics and physical mechanism of temperature fluctuation; and (3) assess the peaked amplitude of individual fluctuating components and evaluate the impact on the susceptible urban areas.

2. Methodology

2.1 Model Configuration

The Advanced WRF (ARW version 3.6.1) [29] was used to examine the fluctuation of meteorological vatiables during a heatwave event (0000 LST on June 23, 2016 to 2400 LST on June 27, 2016) [30]. The simulation was started at 0800 LST on June 21, 2016 for a 40-hour spinning up [31]. During these extremely hot days, the recorded hotest temperature was 35.5 °C at 1400 LST on June 25, 2016. The WRF domain consisted of four one-way nested domains at 9 km (241×181 grids), 3 km (271×181), 1 km (241×181), and 0.33 km (241×181) spatial resolution (Figure 1). The vertical coordinate was composed of 51 η levels from the ground to 50 hPa for the atmospheric model in which the urban canopy was refined to 10-m resolution. The initial and boundary conditions for the atmospheric model were derived from the European Centre for Medium-Range Weather Forecasts (ECMWF) ERA-Interim data whose spatial and temporal resolutions were 0.75° and 6 hr, respectively.

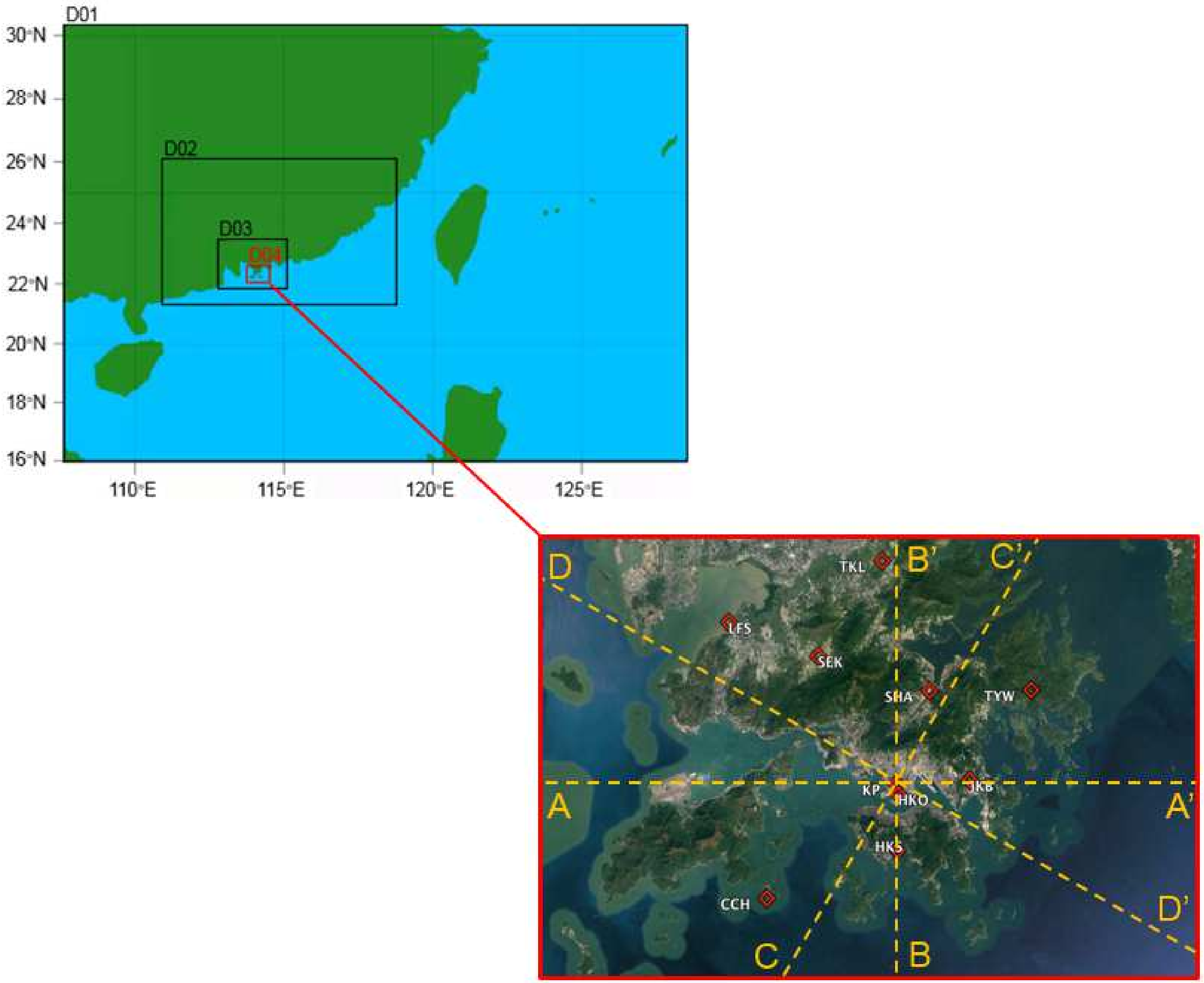

Figure 1. Nested computation domains D01, D02, D03, and D04.

132

To calculate the spatio-temporal variations of meteorological vatiables more accurately, we developed a new landuse/landcover (LULC) map which consisted of 30 urban classes (LCZBC). This new map was generated by combining the local climate zone (LCZ) [32] defined in the World Urban Database and Access Portal Tools (WUDAPT) and the building categories (BCs; 10-m resolution) [33] from the Land Utilization Map of Planning Department (PlanD) of HK Special Administrative Region (HKSAR; Figure 2). In each of the 10 LCZ urban types existing in HK, the landuse was further sub-classified into three BCs (commercial, residential, and non-building; Table 2) according to the dominant LULC at individual model grids. The physical parameterlization schemes used in the current WRF model are tabulated in Table 1. Among them, the combined multi-layer urban canopy model, which was based on BEP/BEM, was used for the built-environment parameterizaton.

Table 1. Physical parameterization schemes used in the WRF model.

Physics Options	Schemes	References
Boundary Layer	BouLac	[34]
Microphysics	Single-Moment 3-class	[35]
Land Surface	Noah	[36]
Cumulus (only in Domain 01)	Kain-Fritsch	[37]
Short Wave Radiation	Dudhia	[38]
Long Wave Radiation	Rapid Radiative Transfer Model	[39]
Surface Urban	BEP/BEM	[25, 26]

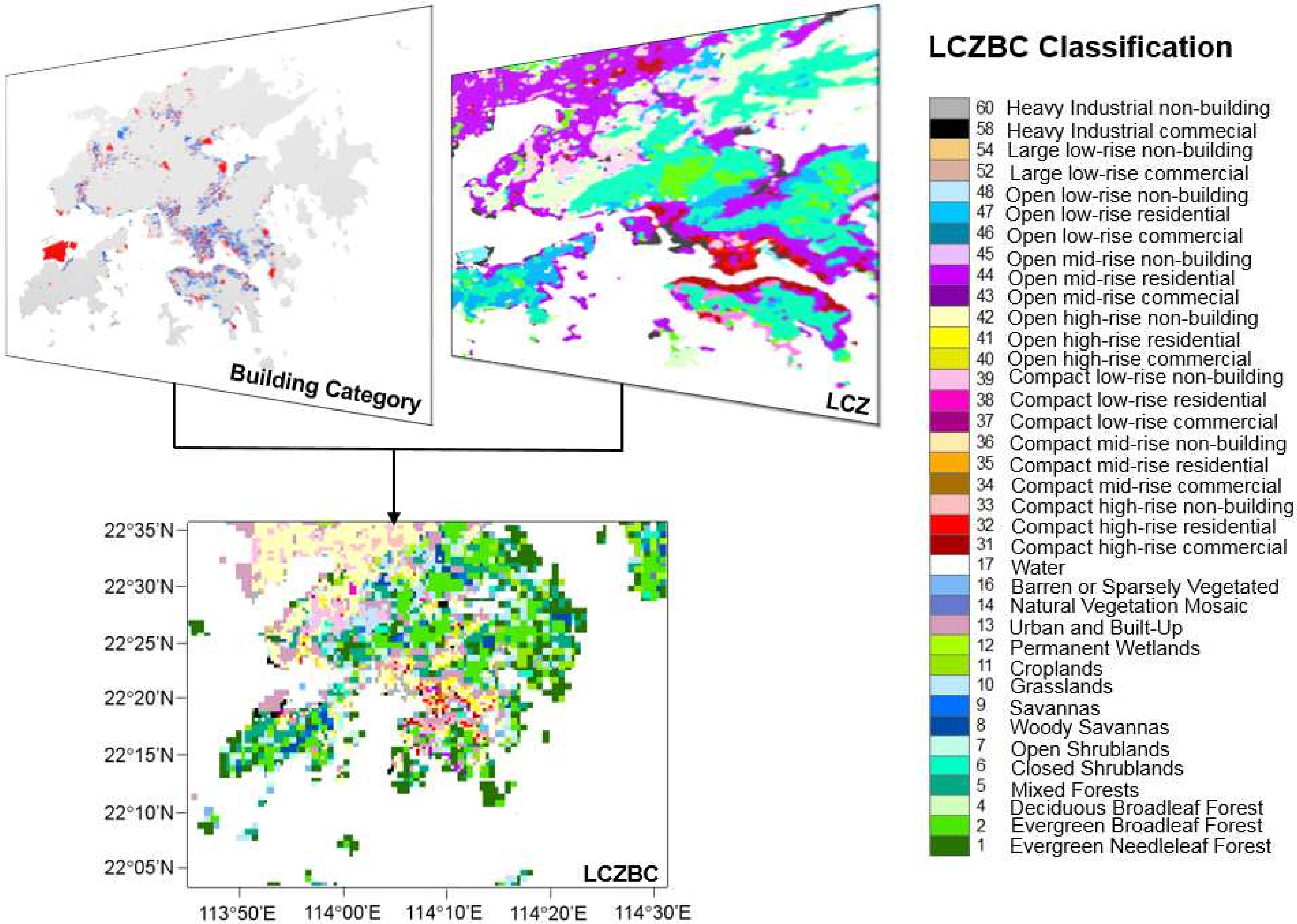

Figure 2. Map of local climate zone and building category (LCZBC) in Hong Kong (HK).

146

Table 2. Sub-classification of local climate zone (LCZ) based on building category (BC) [40].

LCZBC Map – Urban Land Use	**LCZ1** Compact high-rise	LCZ1-C	Compact high-rise Commercial
		LCZ1-R	Compact high-rise Residential
		LCZ1-N	Compact high-rise Non-building
	LCZ2 Compact mid-rise	LCZ2-C	Compact mid-rise Commercial
		LCZ2-R	Compact mid-rise Residential
		LCZ2-N	Compact mid-rise Non-building
	LCZ3 Compact low-rise	LCZ3-C	Compact low-rise Commercial
		LCZ3-R	Compact low-rise Residential
		LCZ3-N	Compact low-rise Non-building
	LCZ4 Open high-rise	LCZ4-C	Open high-rise Commercial
		LCZ4-R	Open high-rise Residential
		LCZ4-N	Open high-rise Non-building
	LCZ5 Open mid-rise	LCZ5-C	Open mid-rise Commercial
		LCZ5-R	Open mid-rise Residential
		LCZ5-N	Open mid-rise Non-building
	LCZ6 Open low-rise	LCZ6-C	Open low-rise Commercial
		LCZ6-R	Open low-rise Residential
		LCZ6-N	Open low-rise Non-building
	LCZ7 Lightweight low-rise	LCZ7-C	Lightweight low-rise Commercial
		LCZ7-R	Lightweight low-rise Residential
		LCZ7-N	Lightweight low-rise Non-building
	LCZ8 Large low-rise	LCZ8-C	Large low-rise Commercial
		LCZ8-R	Large low-rise Residential
		LCZ8-N	Large low-rise Non-building
	LCZ9 Sparsely built	LCZ9-C	Sparsely built Commercial
		LCZ9-R	Sparsely built Residential
		LCZ9-N	Sparsely built Non-building
	LCZ10 Heavy industry	LCZ10-C	Heavy industry Commercial
		LCZ10-R	Heavy industry Residential
		LCZ10-N	Heavy industry Non-building

2.2 Analytical Approach

2.2.1 Empirical Mode Decomposition

The wind-speed and temperature fluctuations in urban areas are complicated by synoptic weather conditions, diurnal variations, and local forcing (e.g. terrain, surface properties, urban morphology, and anthropogenic heat). To examine how these processes influence ground-level winds, HHT was used to decompose the meteorological time series obtained from the WRF-BEP/BEM model. HHT is a time-frequency analysis that consists of two steps. The first step applies EMD to decompose any multi-scale, non-linear time-series data into a finite number of IMFs. IMFs admit well-behaved HHT and reveal the timescales that comprise the dataset. However, EMD often causes mode-mixing, unavoidably leading to the overlapping of IMF spectra. We hence used an improved approach called noise-assisted multivariate EMD (NA-MEMD) [41] instead. The second step is HHT that extracts the instantaneous frequency and amplitude of each IMF. The Hilbert spectrum signifies the time-frequency behavior of amplitude that represents the energy distribution among different physical processes.

2.2.2 Two-point Correlation

To quantify the spatial scales of individual IMFs, two-point correlation

$$C_{\psi}\left(x,r\right)=\frac{\overline{\psi\left(x,t\right)\psi\left(x+r,t\right)}}{\sigma_{\psi}\left(x\right)\sigma_{\psi}\left(x+r\right)} \quad (1)$$

of the wind speed or temperature is calculated between neighboring model grids. Here, x is the reference location, $x+r$ the location at distance r measuring from x, and σ_{ψ} the standard deviation of variable ψ. Two-point correlation $C_{\psi}\left(x,r\right)$ signifies if the variable ψ at two model grids (distance apart = r) experiences coherence in their time series. Specifically, for each model grid, the correlation to its neighboring grids (distance apart = r) is calculated as the average in four cardinal directions (east, south, west, and north). The distance apart r is set as the integer multiple of model spatial resolution of the innermost domain (0.33 km). The two-point correlation is in the range $-1 \leq C_\psi \leq 1$ in which the larger $\left|C_\psi(x,r)\right|$ signifies stronger spatial correlation.

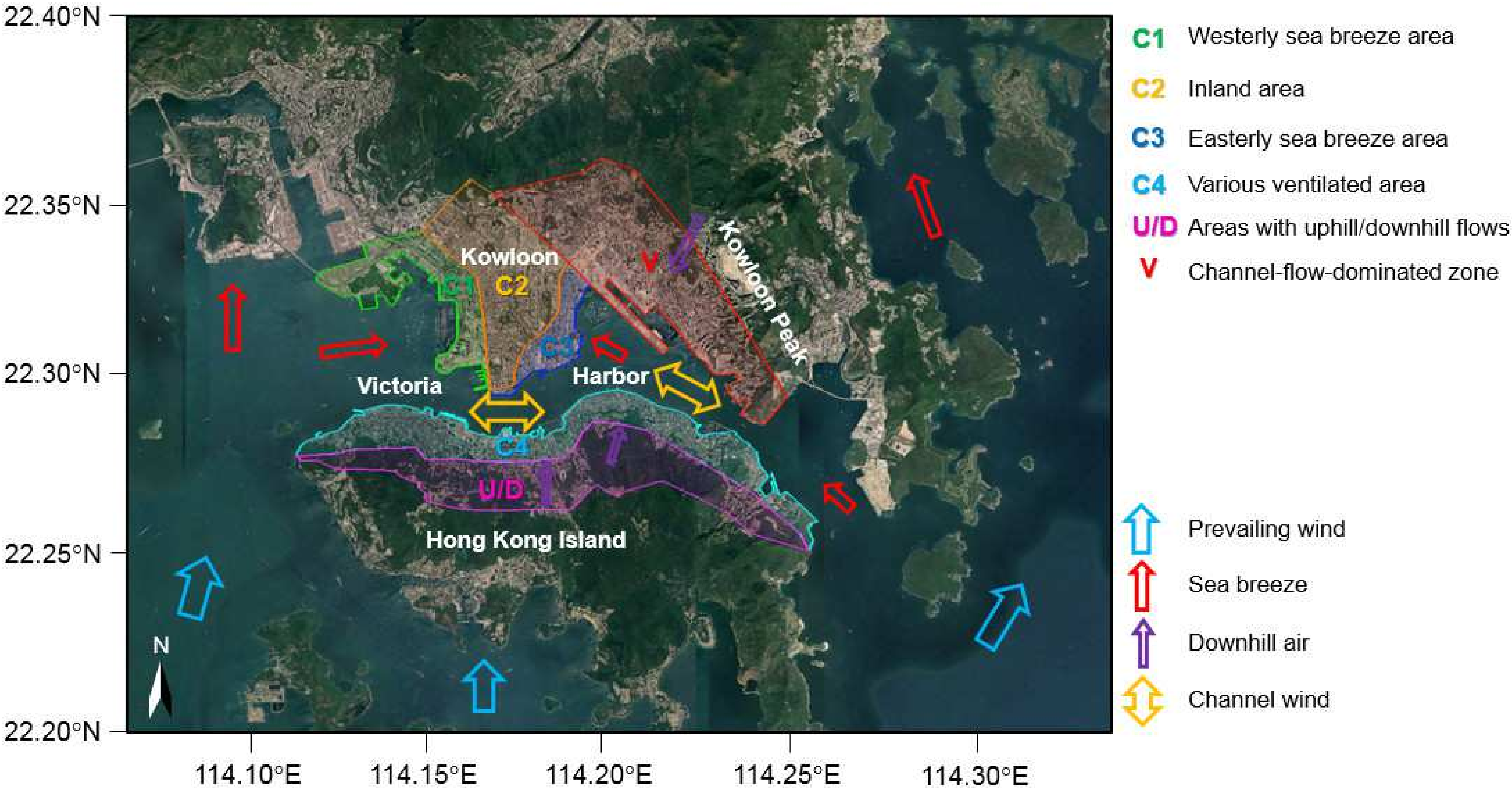

Figure 3. Wind information layer, Urban Climatic Analysis Map (UC-AnMap), of Hong Kong (HK) in summer [42].

174

Table 3. Design of numerical experiments.

Scenario		Numerical experiment	Model setup
Real	1	REAL	WRF coupled to BEP/BEM with the combined data of Local Climate Zone (LCZ) and Building Category (BC; LCZBC) as the landuse and landcover (LULC) configuration.
Hypothetical	2	ALLGREEN	Same as REAL but all the urban areas in the domain D04 are switched to grassland.
	3	NoAC	Same as REAL but all the air-conditioners are switched off.

2.2.3 Wind Information Layer

The schematic of summer wind information was collected from the Urban Climatic Analysis Map (UC-AnMap) of HK (Figure 3) [42]. It illustrates the typical wind patterns during summertime (June to August). The prevailing southerly wind coincides with southerly sea breeze that could penetrate to North HK Island [43]. Besides, sea breezes were observed on the east and west of Kowloon Peninsula. The rugged terrain flanks a narrow inlet to the east of Victoria Harbor, inducing the easterly channel flows [44, 45]. Besides, the mountain/hills caused the uphill/downhill flows from Kowloon Peak or the hilly region in HK Island. UC-AnMap divides the North HK Island and Kowloon Peninsula into 6 zones according to their dominant ventilation characteristics. They are Westerly sea breeze area (C1), Inland area (C2), Easterly sea breeze area (C3), Various ventilated area (C4), Areas with uphill/downhill flows (U/D), and Channel-flow-dominated zone (V).

2.2.4 Numerical Experiment

The sensitivity of (fluctuating) meteorological variables to various local factors, such as terrain and building morphology, was tested by three numerical experiments, including one real scenario (REAL) and two hypothetical scenarios (ALLGREEN, and NoAC; Table 3). The two hypothetical scenarios are: (1) a no-urban scenario (ALLGREEN) by switching all the urban areas in (the innermost) domain D04 (Figure 1) to grassland and (2) a scenario (NoAC) by switching off all the ACs in the urban areas.

2.3 Model Validation

The current WRF modeling results are validated against the measurements from ten selected weather stations of Hong Kong Observatory (HKO; Figure 1). The root-mean-square errors (RMSEs) of 2-m air temperature (*T*2), 2-m relative humidity (*RH*2), and 10-m wind speed (*W*10) are calculated to evaluate the model performance (Table 4). The WRF results and the HKO measurements agree well with each other, demonstrating the reliability of the current WRF-LCZBC model. Specifically, the RMSEs of *T*2 at all the stations (0.91 °C ≤ RMSE ≤ 1.4 °C) are compatible with those of previous WRF studies [46-49]. The uncertainty of *T*2 is quite uniform in the urban (1.04 °C ≤ RMSE ≤ 1.4 °C), suburban (0.91 °C ≤ RMSE ≤ 1.05 °C), and rural (1.25 °C ≤ RMSE ≤ 1.31 °C) areas. The WRF-calculated *RH*2 is more accurate in the rural (8.42% ≤ RMSE ≤ 9.02%) than urban (9.83% ≤ RMSE ≤ 9.89%) and suburban (7.09% ≤ RMSE ≤ 11.16%) sites. Moreover, the maximum *RH*2 RMSE (11.16%) is consistent with that of prior WRF studies over 10 cities in China. The calculation of *W*10 at all the stations is acceptable as well according to the benchmark of European Environment Agency (RMSEs of *W*10 < 2 m sec^{-1}) [50]. Whereas, it is more accurate in rural sites (0.88 m sec^{-1} ≤ RMSE ≤ 1.06

m sec^{-1}) than urban (1.10 m sec^{-1} ≤ RMSE ≤ 1.38 m sec^{-1}) and suburban (0.79 m sec^{-1} ≤ RMSE ≤ 1.41 m sec^{-1}) sites.

In addition, two benchmarks are employed to assess the accuracy of wind direction. The first criterion is suggested by United States Environmental Protection Agency (USEPA) for the mean error (*BIAS*) of wind direction which is calculated as

$$BIAS = \frac{1}{n}\sum_{i=1}^{n}\left|M_i - O_i\right| \tag{2}$$

where M_i and O_i are the modeled and observed values, respectively, and n the number of data points. This criterion is proposed for complex simulation conditions in which $BIAS \leq 55^{o}$ is suggested [51]. Hong Kong is a coastal city with complex terrain where 70% of the total area is hilly topography with mountains, urban, and coastal water intersect. The mountainous flows, land/sea breeze, and urban/rural circulations co-exist, forming a complicated dynamical system (Figure 3). Hence, this criterion is applied to the current model.

The second criterion is developed for areas with complex topography and frequent low-wind-speed conditions [52]. It includes mean wind speed to formulate a benchmark for the gross error of wind direction which is calculated by

$$BIAS_{dir} = \frac{\sum_{i=1}^{n}\min\left(\left|M_i - O_i\right|, \left|M_i - O_i + 360\right|, \left|M_i - O_i - 360\right|\right)}{n} \tag{3}$$

that should fulfill the following requirement

$$BIAS_{dir} \leq \frac{46}{Max(\overline{u}, 0.5)} + 25 \tag{4}$$

where $\bar{u}$ is the mean wind speed. The WRF-calculated wind direction is validated against the observations (Table 4). Apparently, the current WRF model setup met both the criteria above over all the monitoring sites.

Among others, there is a larger deviation of wind direction at the SEK, SHA, and HKS sites where the geographical configurations are quite similar: (1) surrounded by mountain on three sides, (2) in coastal areas, and (3) suburban areas would increase sensible heat and subsequent buoyant flows (Figure 1). These conditions collectively complicate the local-wind systems that enlarge the uncertainty in simulation.

The validation of the current WRF model was detailed in our previous study [40]. The numerical output could accurately represent the weather conditions as well as the urban contexts in HK.

3. Results and Discussion

3.1 Spatio-temporal Scales

The NA-MEMD (Section 2.2.1) was used to analyze the temperature trend at each model grid (2 m or 10 m above ground surface). Here, the reference urban site (HKO) [54] was adopted to demonstrate the data processing. The 5-day hourly time series of 2-m temperature ($T2$) and 10-m wind speed ($W10$) were decomposed into 6 IMFs ($IMF\theta1$ to $IMF\theta6$ for temperature and $IMFW1$ to $IMFW6$ for wind speed) and the residuals (Figure 4).

Table 4. Root-mean-square errors (RMSEs), mean error (*BIAS*) and gross error ($BIAS_{dir}$) between the predicted and observed 2-m temperature (*T*2), 2-m RH (*RH*2), 10-m wind speed (*W*10), and wind direction at the 10 selected weather stations operated by HKO [51-53]

Station	Classification	LCZ type	RMSEs			Mean Error (º)		Gross Error (º)	
			*W*10 (m sec^{-1})	*RH*2 (%)	*T*2 (°C)	*BIAS*	Benchmark	$BIAS_{dir}$	Benchmark
HKO	urban	LCZ1	1.38	9.83	1.4	48.85	55	46.43	49.21
KP	urban	LCZ4	1.10	9.89	1.04	41.87	55	41.87	48.94
HKS	suburban	LCZ5	1.20	8.15	1.05	52.85	55	52.17	58.07
JKB	suburban	LCZ4	0.79	9.8	0.96	45.27	55	41.03	59.82
LFS	suburban	LCZ4	1.41	9.7	0.98	37.86	55	33.16	40.06
SEK	suburban	LCZC	1.07	11.16	1.02	50.35	55	60.88	89.49
SHA	suburban	LCZ6	1.18	7.09	0.91	53.68	55	56.30	57.04
CCH	rural	LCZA	1.06	9.02	1.25	34.14	55	31.13	37.08
TKL	rural	LCZ6	0.88	8.90	1.31	49.51	55	47.33	63.17
TYW	rural	LCZ4	/	8.42	1.30	/	55	/	/

248

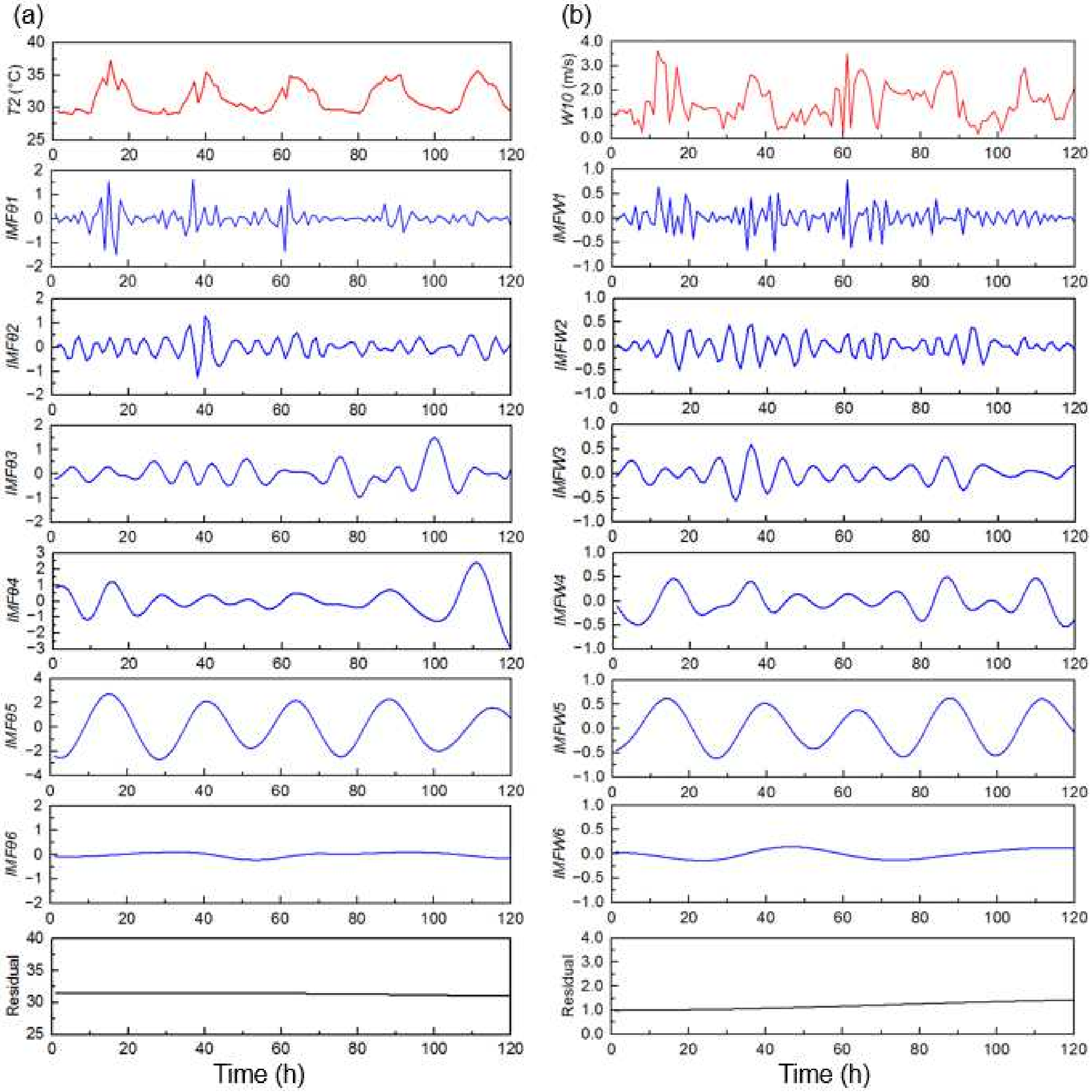

Figure 4. Time series of the original signals (raw data from WRF; red solid lines) as well as the IMFs (blue solid lines) of (a) 2-m temperature *IMFθj* and (b) 10-m wind speed *IMFWj* after NA-MEMD at the HKO (reference) station.

The Hilbert spectra (Figure 5) calculated from the time-series data of *T*2 and *W*10 show that the time-frequency domain could be divided into several parts: synoptic (frequency = 0.0167 cycles hr^{-1}; period = 59.88 hr), diurnal-cycle (frequency = 0.042 cycles hr^{-1}; period = 23.9 hr), and local (0.083 cycles hr^{-1} ≤ frequency ≤ 0.31 cycles hr^{-1}; 2.94 hr ≤ period ≤ 12.04

hr) windows [55]. The temperature component *IMFθ*6 in the synoptic window is moderate that is low-frequency (0.0167 cycles hr^{-1}) and small-amplitude (0.45 °C). It is attributed to the mild fluctuating synoptic conditions during the analysis period [30]. IMF5 in the diurnal-cycle window (*IMFθ*5) is dominated by solar radiation. It is rather periodic (24 hours) that improves the prediction accuracy. The components in these two windows (synoptic and diurnal-cycle) rarely cause temperature anomalies (less risky) because they are driven by the natural atmospheric cycles. As such, this study focuses on IMF1 to IMF4 in local windows in which intense temperature fluctuations are likely to occur due to human activities and anthropogenic heat release.

To define the temporal scales of IMFs in local windows, the marginal spectra are derived by integrating the amplitude in HHT spectra over the entire temporal domain. Figure 6 shows the spatial average of marginal spectra of *T*2 and *W*10. Here, the spatial average is the average of all model grids (2 m or 10 m above ground surface) in the domain D04 (Figure 1). The abscissa depicts the dominant frequencies of individual IMFs which are the inverses of their time scales. The (dominant) time scales of IMF1, IMF2, IMF3, and IMF4 in *T*2 (*W*10) are 2.63 hr (2.53 hr), 5.88 hr (5.78 hr), 13.16 hr (9.84 hr) and 22.72 hr (19.05 hr), respectively.

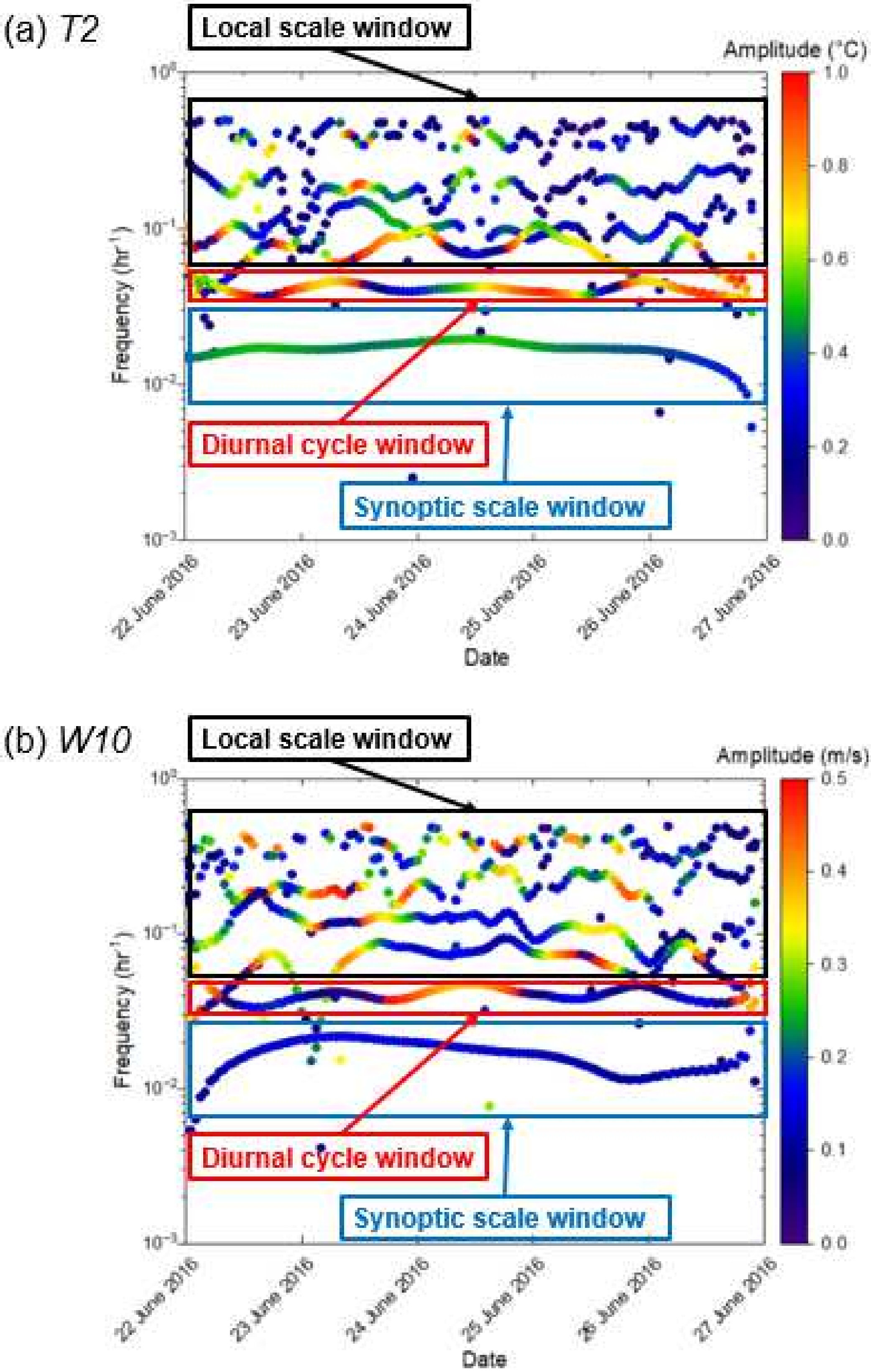

Figure 5. Hilbert-Huang transform (HHT) spectra of (a) 2-m temperature *T*2 and (b) 10-m wind speed *W*10 at the HKO station (reference) during the heatwave event.

271

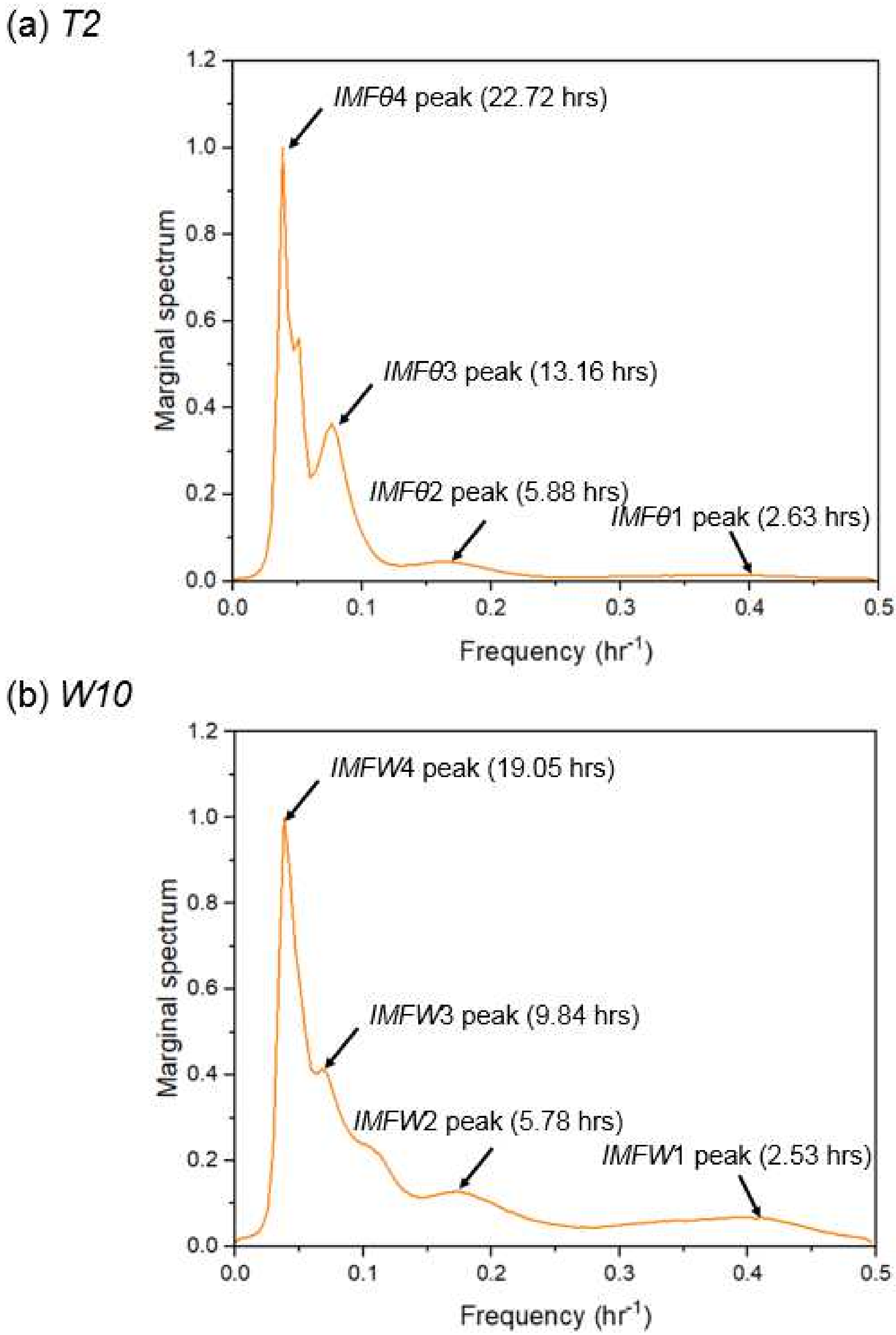

Figure 6. Hilbert-Huang transform (HHT) marginal spectra of (a) 2-m temperature *T*2 and (b) 10-m wind speed *W*10 at the HKO station during the heatwave event.

The spatial scales of the IMFs in local-scale window were calculated by the two-point correlation (Section 2.2.2). The ensemble averaged spatial coherence drops with increasing the distance between the two model grids (Figure 7). Here, the ensemble average is the spatio-temporal average of all model grids (2 m or 10 m above ground surface) in domain D04 (Figure 1). The e-folding correlation (e^{-1}) distance was used to define the spatial scale of each component [56]. The spatial scales of IMF1, IMF2, IMF3, and IMF4 in $T2$ ($W10$) are 2.31 km (0.99 km), 4.29 km (1.65 km), 5.94 km (2.64 km), and 6.6 km (2.97 km), respectively.

3.2 Physical Explanation

The physical significance of IMF2 of 2-m temperature ($IMF\theta 2$) and 10-m wind speed ($IMFW2$) is explored by comparing their amplitudes in the foothill areas (U/D and V zones; Figure 3) and the inland area (C2 zone) for the REAL scenario (Table 3). Figure 8 compares the diurnal variation of the spatial average of $IMF\theta 2$ and $IMFW2$ in these climate areas. Here, the spatial average is the average of all model grids (2 m or 10 m above ground surface) in a specific climate area (U/D, V or C2). The temperature $IMF\theta 2$ and wind speed $IMFW2$ in the foothill areas (0.23 °C and 0.18 m sec^{-1} in U/D zones; 0.33 °C and 0.16 m sec^{-1} in V zones) tend to be larger in amplitudes than those in the inland area (0.19 °C and 0.11 m sec^{-1}). It is thus implied that $IMF\theta 2$ and $IMFW2$ possess more intense fluctuations in the foothill areas than their inland-area counterparts. It could be attributed to the mountains surrounding the foothill areas that induce channeling/uphill/downhill winds, strengthening the atmospheric turbulence.

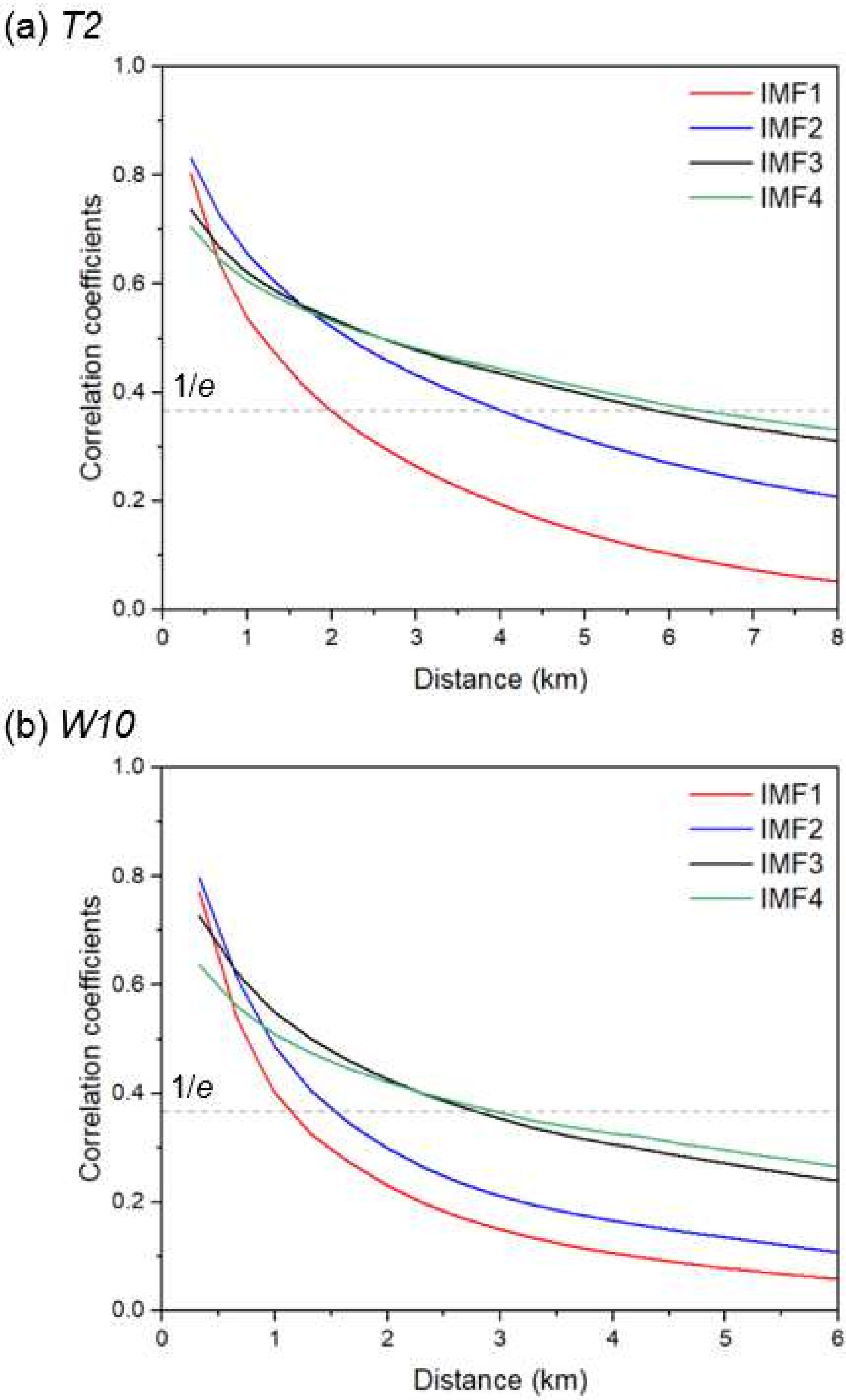

Figure 7. Average spatial coherence of (a) 2-m temperature *T*2 and (b) 10-m wind speed *W*10 during the heatwave event.

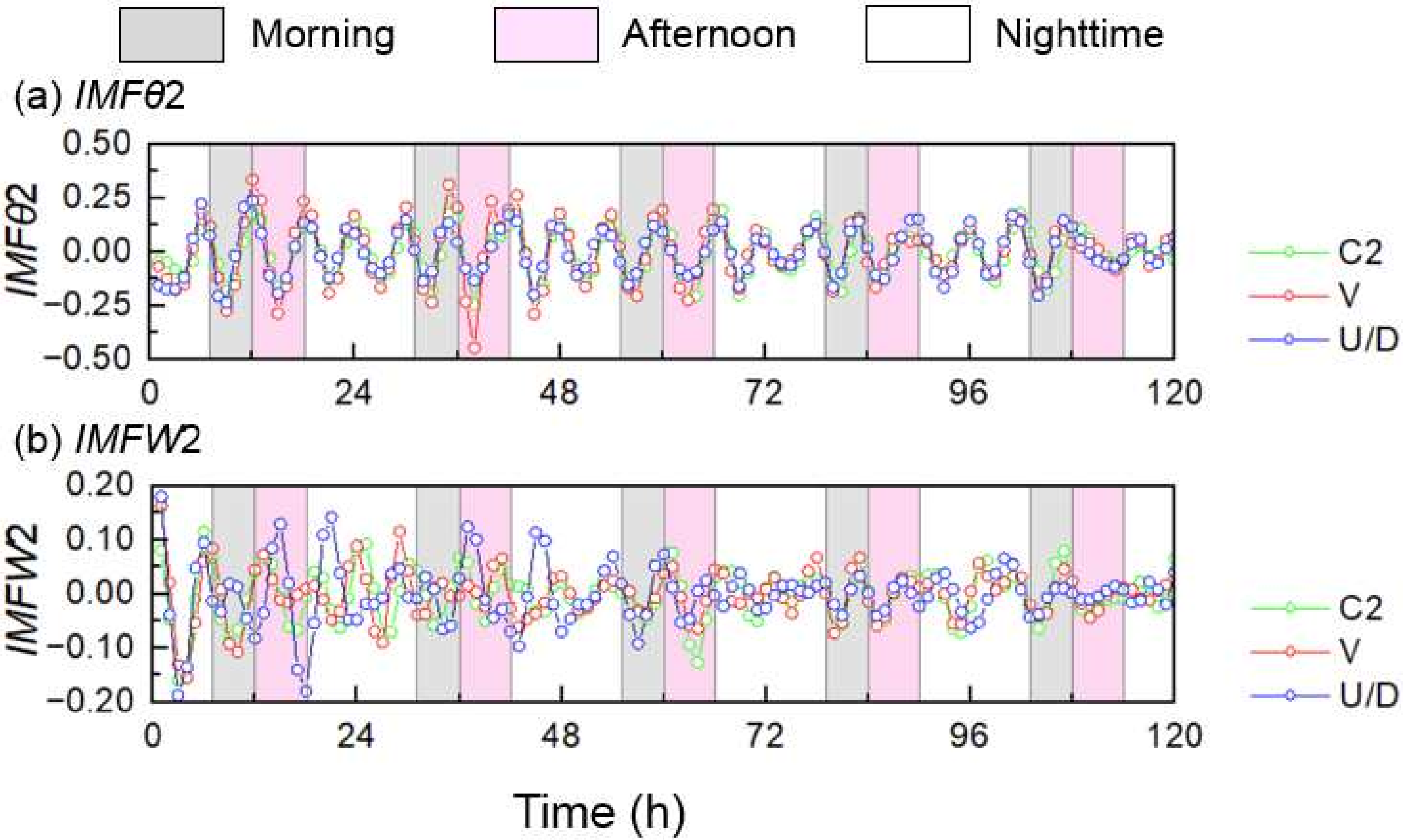

Figure 8. Time series of spatially averaged IMF2 of (a) 2-m temperature *IMFθ*2 and (b) 10-m wind speed *IMFW*2 in inland (C2) and foothill (V and U/D) areas.

294

To investigate the physical mechanism behind IMF3 in 2-m temperature $IMF\theta3$ and 10-m wind speed $IMFW3$, two numerical experiments were conducted for REAL and ALLGREEN scenarios (Table 3). The surface roughness and the sensible heat flux in ALLGREEN are lower compared with those in REAL. It results in the faster spatially averaged $W10$ and the cooler spatially averaged $T2$ in ALLGREEN than REAL. The amplitudes of IMF3 in coastal (C1 and C3 zones; Figure 3) and inland (C2 zone) areas are compared for the REAL scenario. By and large, the fluctuating $IMF\theta3$ and $IMFW3$ in the coastal areas (1.17 °C and 0.30 m sec^{-1} for C1, 0.95 °C and 0.34 m sec^{-1} for C3; depending on the prevailing direction of sea breeze) are more noticeable than those in inland area (0.91 °C and 0.26 m sec^{-1} for C2; Figures 9c and 9d). It is because the sea breeze in coastal areas introduces disturbance locally that subsequently modifies the IMF3. Besides, there is more intense fluctuation in coastal areas than inland areas in ALLGREEN scenario (Figures 9e and 9f).

The correlation between the IMF3 and the land/sea breeze is further examined by the differences in $IMF\theta3$ ($\Delta IMF\theta3_{C3\text{-}C2}$ and $\Delta IMF\theta3_{C1\text{-}C2}$) and $IMFW3$ ($\Delta IMFW3_{C1\text{-}C2}$ and $\Delta IMFW3_{C3\text{-}C2}$) between the coastal (C1 and C3 zones) and inland (C2 zone) areas. The diurnal variations of $\Delta IMF\theta3$ and $\Delta IMFW3$ for the scenarios REAL and ALLGREEN are compared in Figures 9g to 9j. Unlike the scenario ALLGREEN, higher sensible heat in the urban areas is observed in REAL so is the abrupt land/sea temperature gradient because of the different heat capacities of land and sea surfaces. As such, a larger difference in IMF3 amplitude between the coastal and inland areas is observed in the scenario REAL than that in ALLGREEN. This finding also indirectly suggests that IMF3 is dominated by land/sea breeze.

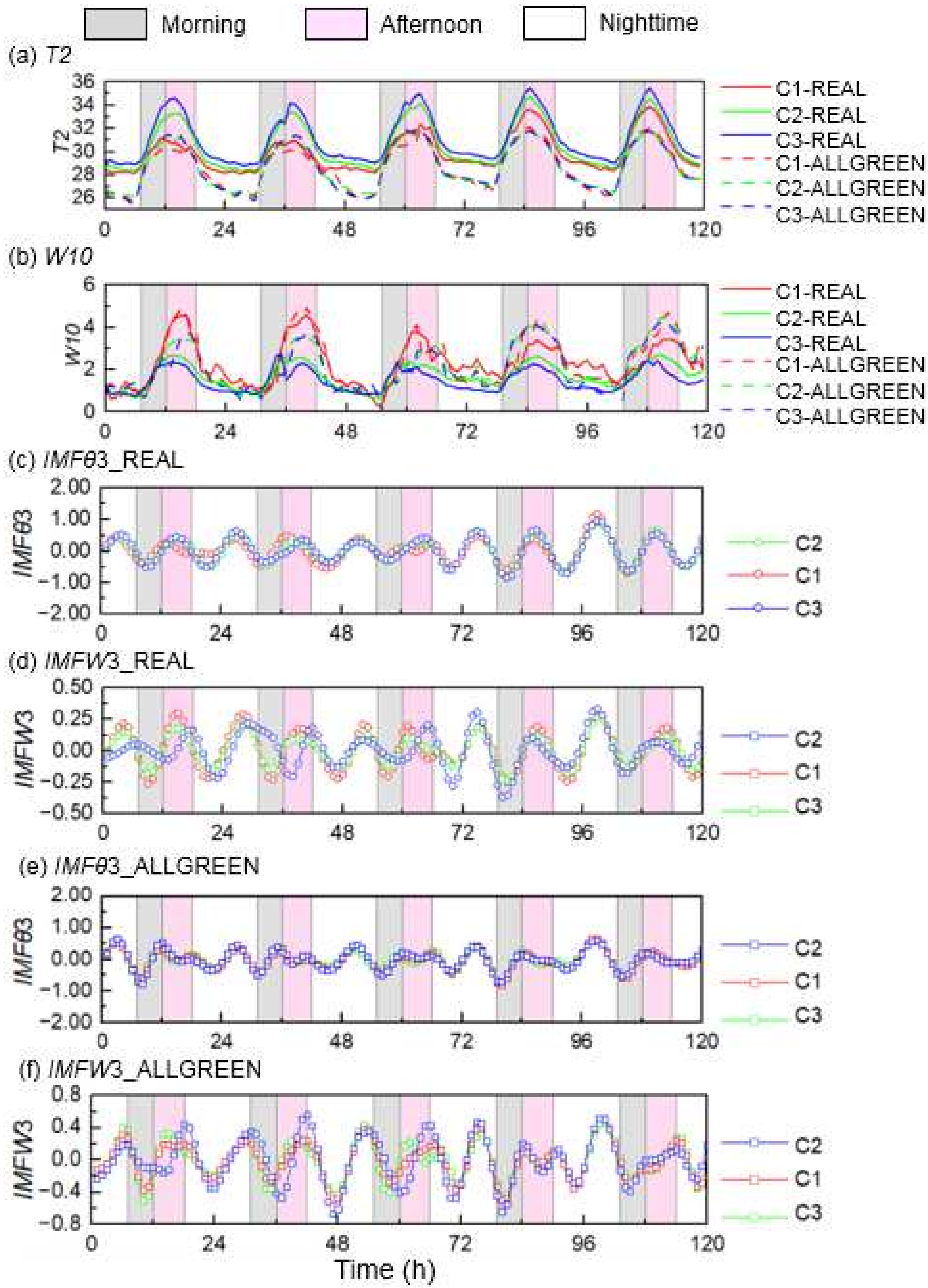
Morning
Afternoon
Nighttime
(a) T2
T2
C1-REAL
C2-REAL
C3-REAL
C1-ALLGREEN
C2-ALLGREEN
C3-ALLGREEN
(b) W10
W10
C1-REAL
C2-REAL
C3-REAL
C1-ALLGREEN
C2-ALLGREEN
C3-ALLGREEN
(c) IMFθ3_REAL
IMFθ3
C2
C1
C3
(d) IMFW3_REAL
IMFW3
C2
C1
C3
(e) IMFθ3_ALLGREEN
IMFθ3
C2
C1
C3
(f) IMFW3_ALLGREEN
IMFW3
C2
C1
C3
Time (h)

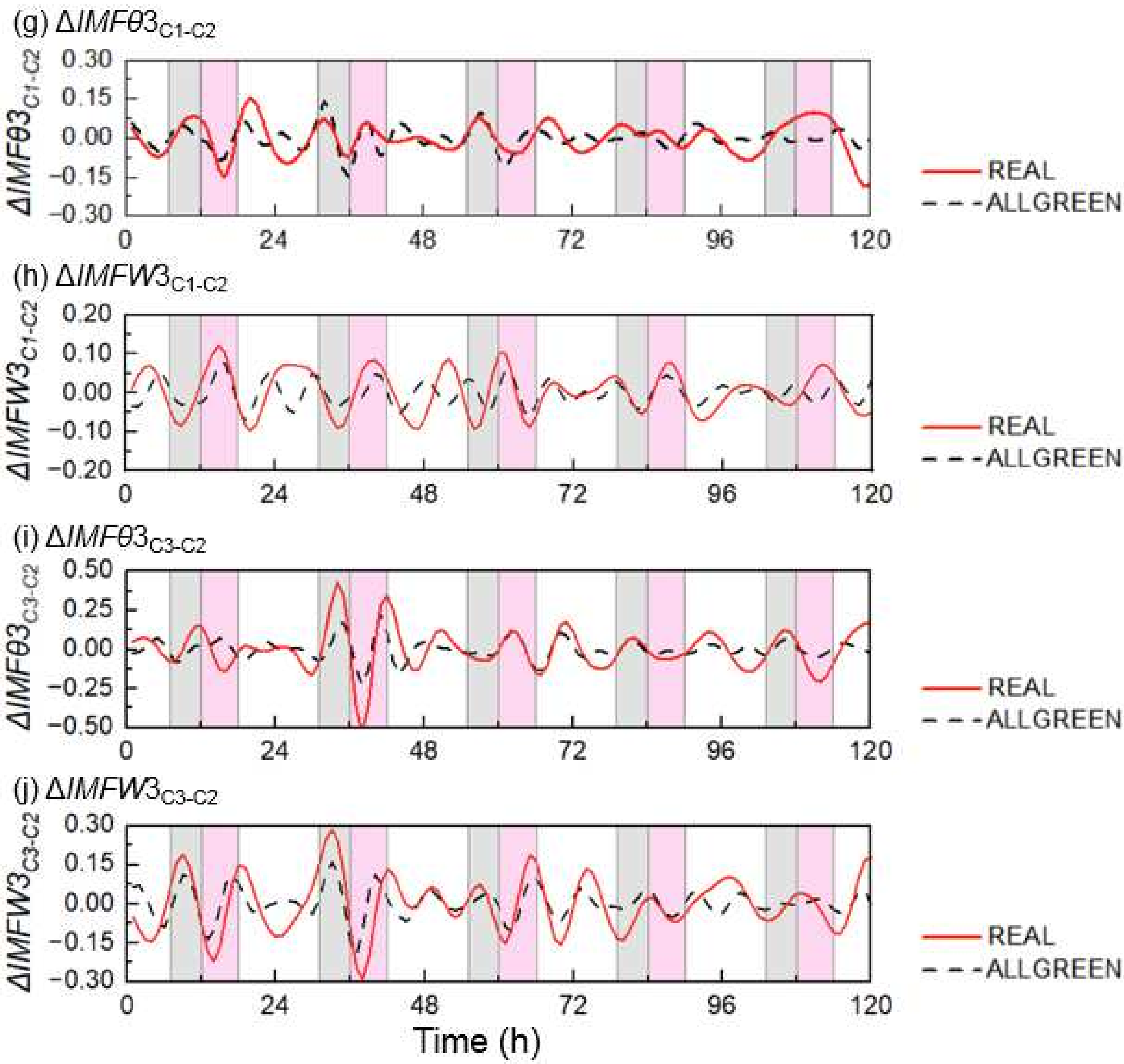

Figure 9. Time series of spatially averaged (a) 2-m temperature $T2$, (b) 10-m wind speed $W10$. (c) 2-m temperature $IMF\theta3$ and (d) 10-m wind speed $IMFW3$ for inland (C2) and coastal (C1 and C3) areas in REAL scenario. (e) 2-m temperature $IMF\theta3$ and (f) 10-m wind speed $IMFW3$ for inland (C2) and coastal (C1 and C3) areas in ALLGREEN scenario. Their differences in (g) 2-m temperature $\Delta IMF\theta3_{\text{C1-C2}}$ and (h) 10-m wind speed $\Delta IMFW3_{\text{C1-C2}}$ between C1 and C2; together with those in (i) 2-m temperature $\Delta IMF\theta3_{\text{C3-C2}}$ and (j) 10-m wind speed $\Delta IMFW3_{\text{C3-C2}}$ between C3 and C2.

The diurnal variation of ensemble-averaged IMF4 in 2-m temperature (*IMFθ*4) and 10-m wind speed (*IMFW*4) for REAL and NoAC scenarios are compared to reveal the physical implication (Figure 10). Their surface roughness is the same but there is more anthropogenic heat in REAL and subsequently more noticeable urban-rural temperature gradient, causing higher spatially averaged *T*2 and *W*10 (Figures 10a and 10b). For daytime *IMFθ*4, solar radiation is the major heating source in urban areas. In this connection, the contribution from anthropogenic heat is insignificant so the amplitudes of *IMFθ*4 in the scenarios REAL and NoAC are comparable (Figures 10c and 10d). Whereas, anthropogenic heat dominates at nighttime, the scenario REAL (0.64 °C, with anthropogenic heat) exhibits a larger amplitude of *IMFθ*4 than does NoAC (0.52 °C, without anthropogenic heat). Besides, there is a larger amplitude of *IMFW*4 in REAL (0.51 m sec^{-1}) than that in NoAC (0.49 m sec^{-1}) for both daytime and nighttime. Furthermore, a time lag is observed in *IMFW*4 in NoAC (about 2 hours) compared with that in REAL. It is induced by the weakened anthropogenic heat exhaust in NoAC that subsequently relieves the disturbance caused by vertical mixing and UHI circulation [31]. These findings in turn suggest that the IMF4 is dominated by the anthropogenic heat in urban areas.

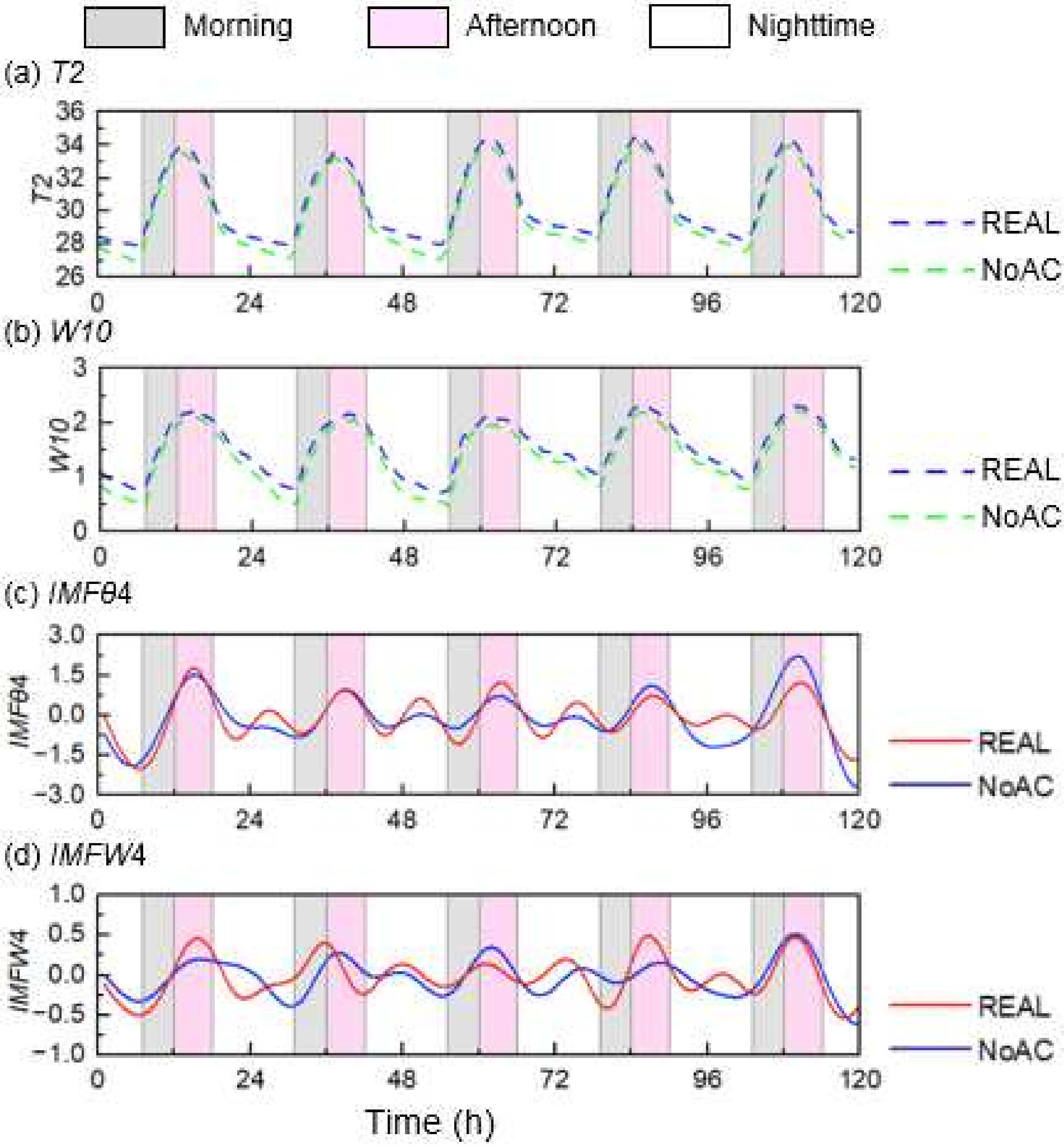

Figure 10. Time series of spatially averaged (a) 2-m temperature *T*2, (b) 10-m wind speed *W*10, IMF4 of (c) 2-m temperature *IMFθ*4 and (d) 10-m wind speed *IMFW*4.

333

The physical implication of IMF1, IMF5, and IMF6 could be explained according to their spatio-temporal scales. The spatial (2.31 km for $IMF\theta 1$ and 0.99 km for $IMFW1$) and the temporal (2.63 hr for $IMF\theta 1$ and 2.53 hr for $IMFW1$) scales of the IMF1 are small that are substantially limited by the buildings and/or streets. Previous efforts had reported that these small-scale fluctuations of temperature and wind are attributed to the heat storage/release [57] in construction material and the turbulence/disturbance in street canyons [8]. Besides, the trend of IMF5 is periodic and stationary (close to the diurnal cycle; temporal scale = 23.9 hr) so it is driven by solar radiation. The frequency and amplitude of the IMF6 during the heatwave event are negligible. The physical process behind is the synoptic forcing [55].

Alike our findings in IMF5 and IMF6, the components with similar frequency were explained by the diurnal-cycle variations and the synoptic scales elsewhere [55]. Whereas, for the first time, the current results differentiate the high-frequency components induced by terrain, land/sea breeze, as well as anthropogenic heat. Afterward, their spatio-temporal characteristics and physical mechanism are elucidated.

3.3 Susceptible Urban Areas

In this section, the effective ranges of those high-frequency IMFs ($IMF\theta 1$ to $IMF\theta 4$) in the local-scale window and the corresponding susceptible urban areas are assessed through their respective peaked amplitudes. The (positive) peaks of $IMF\theta 1$ to $IMF\theta 4$ at z = 2 m above ground surface are extracted from their time series whose spatial distributions are mapped over the central business district of HK (Figure 11).

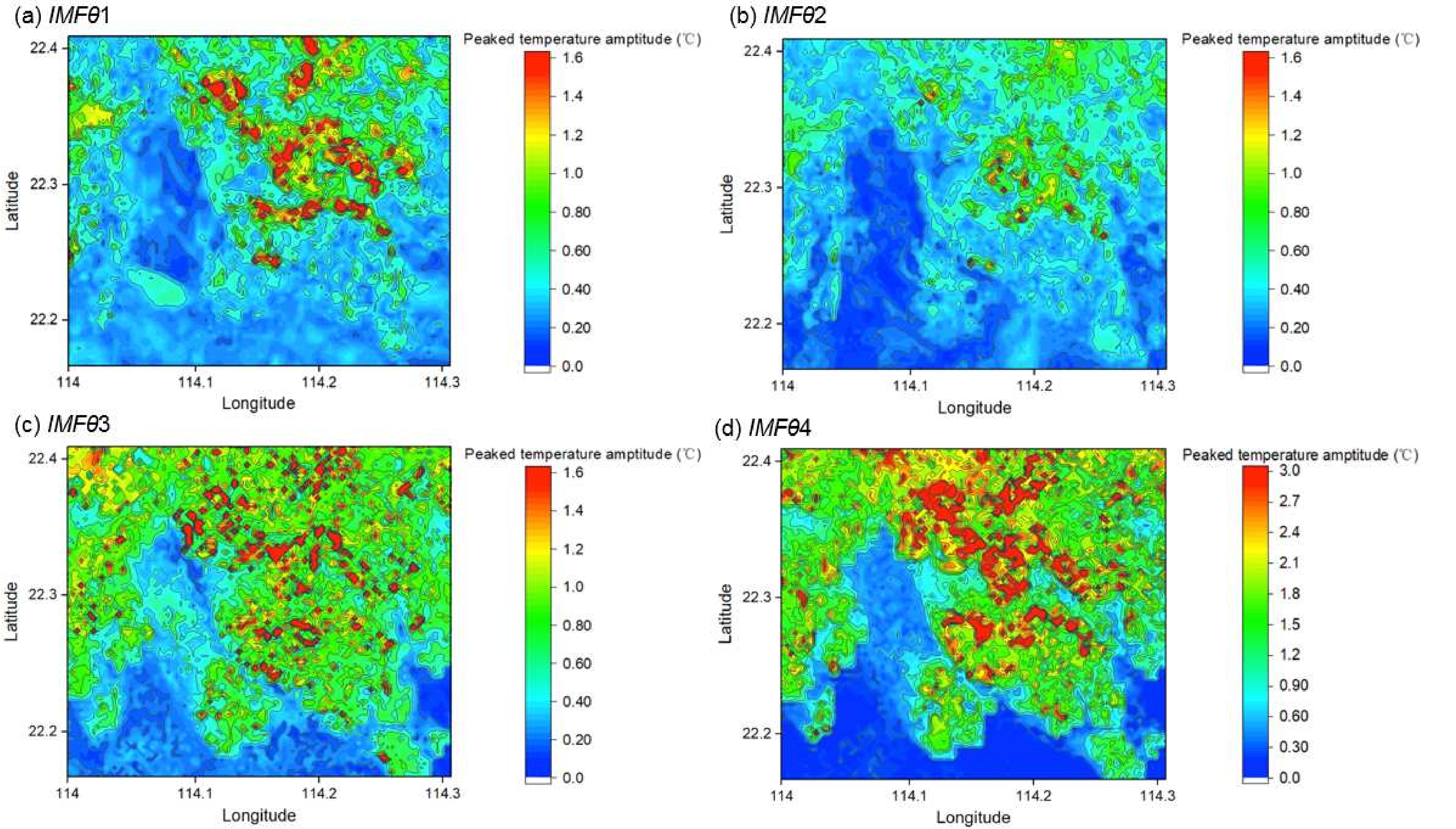

Figure 11. Spatial distribution of the peaked amplitudes of (a) *IMFθ*1, (b) *IMFθ*2, (c) *IMFθ*3, and (d) *IMFθ*4 in the HK central business district.

356

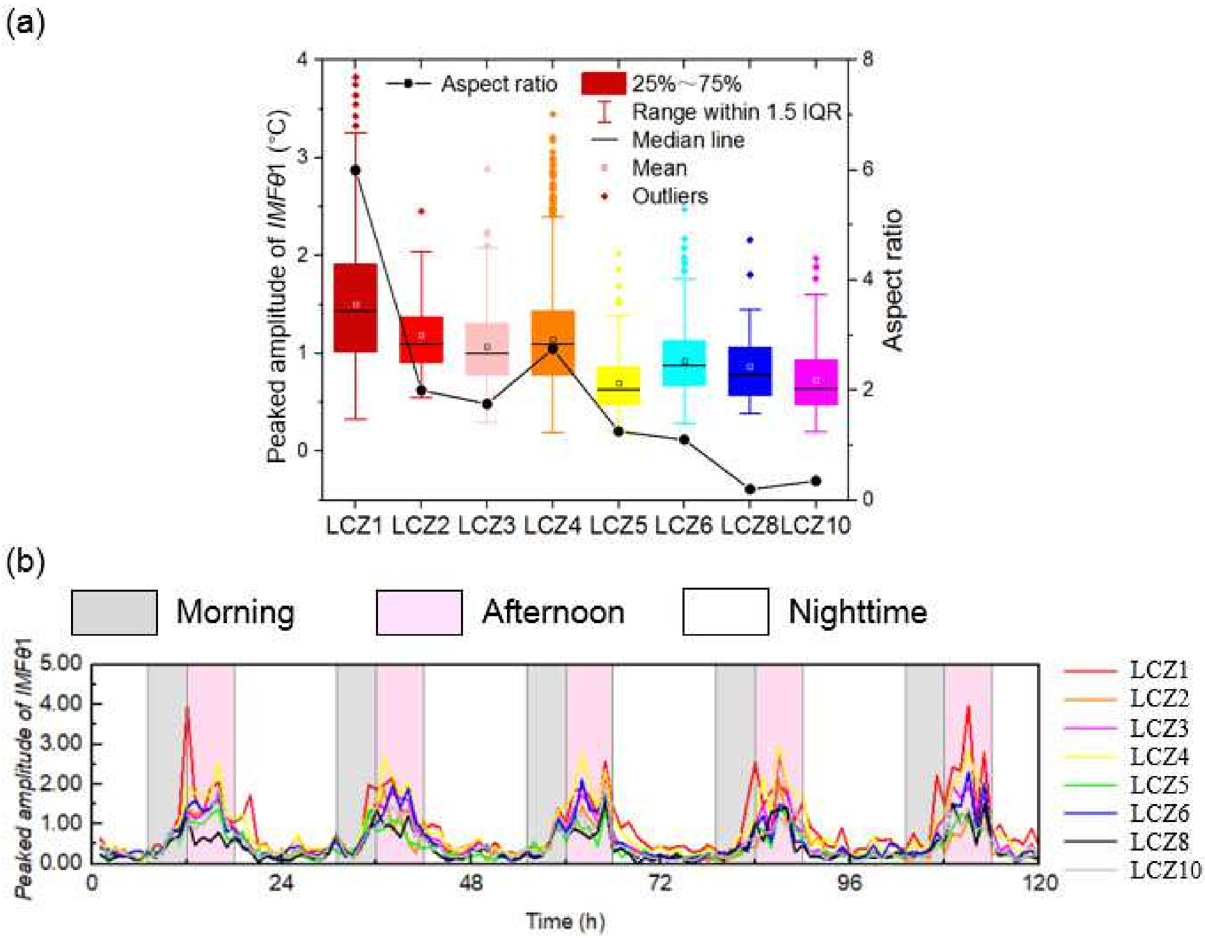

Figure 12. (a) Spatial average of the peaked amplitudes of 2-m temperature *IMFθ*1 and (b) time series of peaked amplitudes of *IMFθ*1for individual LCZs.

The most intense fluctuation of *IMFθ*1 resides in the urban areas (1.4 °C to 1.6 °C). Rural areas, on the contrary, show narrower temperature fluctuations (0.6 °C to 1.0 °C) in the same scale (Figure 11). The distinction and boundary between urban and natural surfaces are clearly defined, concurring the aforementioned physical explanation: disturbance and heat storage/release are related to buildings (Section 3.2). Figure 12a presents the ensemble average of the peaked *IMFθ*1 of each LCZ type. It closely follows the aspect ratios (ARs; building-height-to-street-width) of the LCZ types that demonstrates the importance of urban morphology and building configuration to micro-scale temperature fluctuations. Apparently, urban morphology plays a key role in the temperature fluctuations of compact high-rise (LCZ1) and open high-rise (LCZ4) LCZs where the ARs are high ($2.75 \leq AR \leq 6$). Existing studies also suggest that the heatwave extent is sensitive to urban morphology [58]. Hence, these LCZs likely suffer from the peaked, high-frequency fluctuating temperature $IMF\theta1$. There are two reasons for the elevated $IMF\theta1$ amplitudes: (1) deep street canyons cause more disturbance to winds, and (2) more massive buildings reinforce heat storage/release.

The time series of peaked amplitude in different LCZs are shown in Figure 12b. Urban morphology tends to induce more noticeable peaks in daytime but gentle ones at nighttime. Besides, urban types exhibit the greatest differences at noon and in early afternoon (1200 to 1500 LST). During nighttime, the IMF1 fluctuation is uniform in majority urban areas other than the compact high-rise (LCZ1) areas. Instead, the compact high-rise (LCZ1) areas exhibit the most prominent amplitude of fluctuating temperature which could be up to 3.97 °C in daytime and 1.73 °C at nighttime. It is noted that the peaks in high-rise building areas (LCZ1 and LCZ 4) are sharp and would erect suddenly over 2.98 °C within an hour. It might intensify the fluctuation of power usage, challenging the reliability of power grids. Therefore, urban planners should pay more attention to very high-frequency fluctuating temperature in these areas to mitigate the heat-related risks.

Most of the foothill areas possess the largest amplitude of $IMF\theta2$ (Figure 11). This finding is consistent with the aforementioned physical processes of $IMF\theta2$ (Section 3.2). The disturbance is induced by mountainous terrain and the associated uphill/downhill wind. Besides, the sensitivity of *IMFθ*2 peaked amplitude to the distance measuring from mountain/hill areas is tested in this study (Figure 13a). The grids with the *i*-pixel distance to mountain/hill areas are grouped into the corresponding *i*-th-pixel zones and the average *IMFθ*2 peaked amplitude of individual zone is obtained by:

$$\overline{IMF\theta 2^{\max}{}_{i}} = \frac{\sum_{j=1}^{n} IMF\theta 2^{\max}{}_{ij}}{n} \quad (5)$$

where $IMF\theta 2^{\max}{}_{ij}$ is the *IMFθ*2 peaked amplitude of the *j*-th grid in the *i*-th-pixel zone and *n* the total grid number of the *i*-th-pixel zone. The *IMFθ*2 peaked amplitude gradually reduces with increasing distance measuring from the mountains/hills and their correlation is tight (Figure 13). Eventually, it does not dominate the urban temperature beyond a certain distance. This range (about 8 km) before the *IMFθ*2 peaked amplitude diminishing could be considered the effective distance being influenced by mountainous circulation. These findings signify that the foothill areas within 8-km range are susceptible to the temperature fluctuations caused by slope flows.

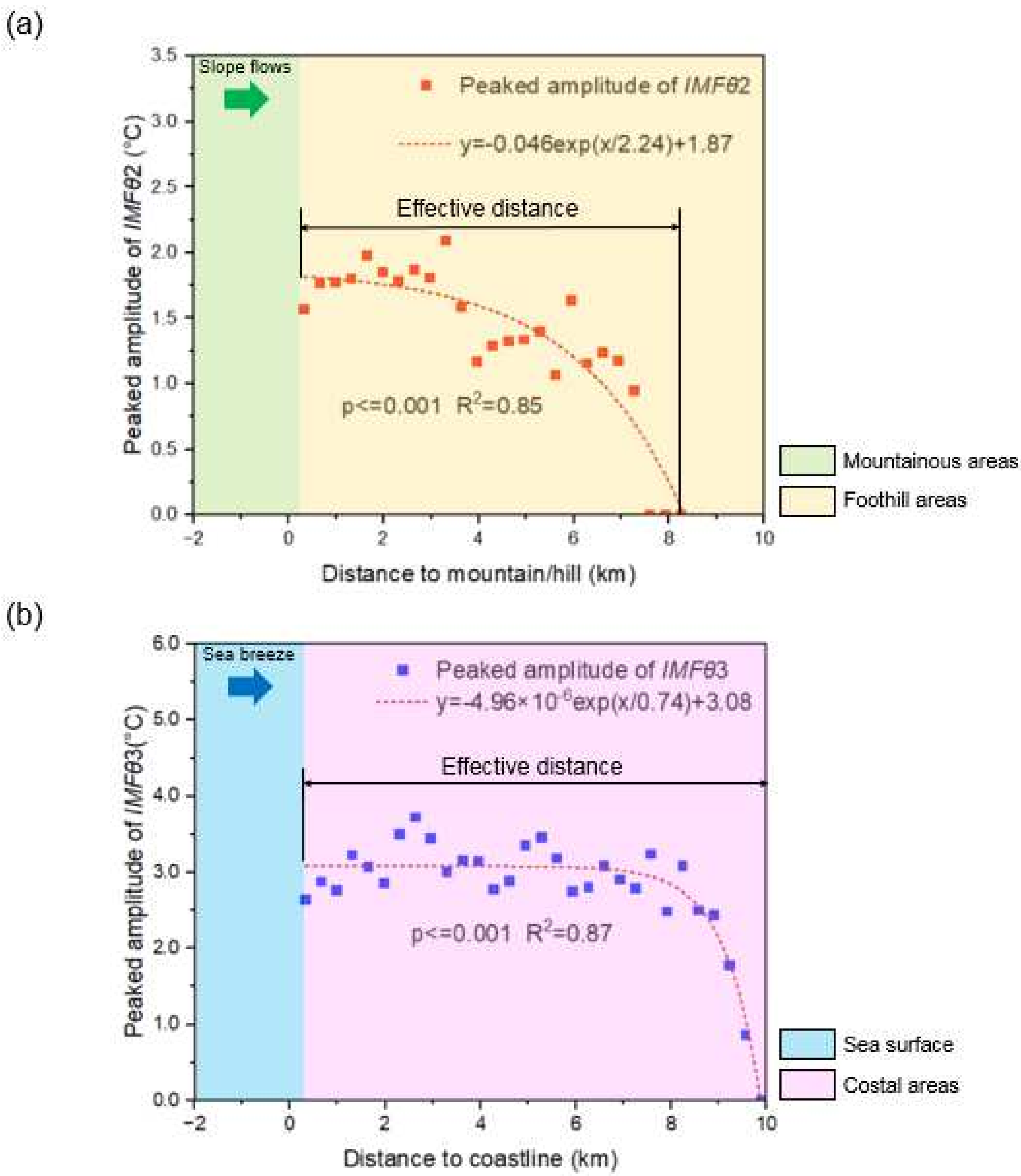

Figure 13. Peaked amplitudes of 2-m temperature of (a) IMF2 $IMF\theta 2$ expressed as the distance to mountains/hills and (b) IMF3 $IMF\theta 3$ expressed as distance to coastline.

$IMF\theta 3$ fluctuates most intensely in coastal areas. Hence, it is associated with the disturbance induced by land/sea breeze. The sensitivity of $IMF\theta 3$ peaked amplitude to the distance measuring (inland) from coastline is tested (Figure 13b). Analogous to $\overline{IMF\theta 2_i^{\max}}$ in

Equation (5), $\overline{IMF\theta 3_i^{\max}}$ is used in the comparison. The temperature fluctuations *IMFθ*3 diminish with increasing distance from the coastline. The effective distance (about 10 km) of *IMFθ*3 is determined based on the trend of the best-fit profile which drops sharply after 8-km away from the coastline. These findings suggest that the areas within 10 km measuring from the coastline are more sensitive to land/sea breeze.

The high-amplitude zones of *IMFθ*4 are mainly located in urban areas (Figure 11). Unlike *IMFθ*1, the distinction in *IMFθ*4 peaked amplitude between urban and rural areas are ambiguous. It could be attributed to the heat dissipation from urban to rural areas such as urban-rural thermal interaction through recirculating winds. In this connection, urban and suburban areas with compact anthropogenic heat sources are more sensitive to the fluctuating temperature *IMFθ*4.

Alike the findings reported in this paper, it was reported elsewhere that the influence of land/sea breeze on urban temperature is weakened with increasing distance from the coastline [59]. Moreover, there exists an effective distance of sea-breeze depending on city properties. As such, it is necessary to examine the relationship between *IMFθ*2 and the distance from marine surfaces.

HHT has been used to analyze the long-term (several decades) urban temperatures previously [15]. Unlike this study, the short-term urban temperatures during a typical heatwave event (within a week) are rarely examined using EMD. Moreover, the peaked amplitude of high-frequency temperature components (temporal period ≤ 24 hr) remains an open question. These components are generally aperiodic and non-stationary. Urban planners often encounter difficulties effectuating remedial measures for power security. Once peaked, these drastic fluctuations would cause the failure of power infrastructure and blackout. Thus, we assess the impacts of these components in response to various urban contexts and examine their effective range as well as susceptible urban areas.

3.4 Effect of Heatwave

Hong Kong Observatory (HKO) [30] and an existing study [31] have defined 0000 LST on June 23, 2016 to 2400 LST on June 27, 2016 as a heatwave event. In June 2016, the maximum temperature of 32.4 ºC was record-high in June [30]. The intensification of the southwest monsoon on June 12, 2016 resulted in windy conditions in the next five days and precipitation until June 18, 2016 [30]. Afterward, the weather changed to sunny and hot on June 19, 2016 when the trough was dissipated and the subtropical ridge dominated over southern China. The pre-heatwave and heatwave were then initiated that persisted for another nine days. In view of the calm winds and the abundant sunshine, HKO recorded four consecutive days with daily maximum temperatures exceeding 35.0 ºC from June 24 to 27, 2016. It was a new record after the previous heatwave event of three consecutive days from May 30 to June 1, 1963 [30]. During the heatwave event being examined in this manuscript, the hottest temperature record was 35.5 ºC at 1400 LST on June 25, 2016. Finally, the heatwave event ended on June 28, 2016 when a low-pressure system with heavy rainfall moved to the coastal area of Guangdong province [30]. The weather stayed hot and rainy for the rest of the month because of southerly (on-shore) winds. In this connection, the weather conditions from June 17 to 28, 2016 were divided into four periods: non-heatwave (June 17 to 18, 2016), pre-heatwave (June 19 to 22, 2016), heatwave (June 23 to 27, 2016), and post-heatwave (June 28, 2016). The WRF-calculated results show that it was hottest in the heatwave period during which the wind speeds were moderate compared with its non-heatwave and pre-heatwave counterparts (Figure 14).

The heatwave effects on individual IMFs are explored by comparing their amplitudes in different periods (Figures 14 and 15). By and large, most air temperature ($IMF\theta1$ to $IMF\theta4$) and minor wind speed ($IMFW3$) components had more intense fluctuations during the heatwave ($IMF\theta1$: 1.49 °C, $IMF\theta2$: 0.83 °C, $IMF\theta3$: 0.81 °C, $IMF\theta4$: 1.18 °C, $IMFW3$: 0.73 m sec^{-1}) and post-heatwave ($IMF\theta1$: 1.16 °C, $IMF\theta2$: 0.29 °C, $IMF\theta3$: 1.36 °C , $IMF\theta4$: 1.71 °C, $IMFW3$: 0.78 m sec^{-1}) periods compared with the pre-heatwave ($IMF\theta1$: 0.81 °C, $IMF\theta2$: 0.50 °C, $IMF\theta3$: 0.86 °C , $IMF\theta4$: 0.61 °C, $IMFW3$: 0.72 m sec^{-1}) and non-heatwave ($IMF\theta1$: 0.31 °C, $IMF\theta2$: 0.29 °C, $IMF\theta3$: 0.38 °C , $IMF\theta4$: 0.34 °C, $IMFW3$: 0.56 m sec^{-1}) periods. The difference is attributed to the substantial spatial temperature gradient in these periods that subsequently strengthens building heat storage/release ($IMF\theta1$), urban-mountain heat exchange ($IMF\theta2$), land/sea breeze ($IMF\theta3$ and $IMFW3$), and anthropogenic heat ($IMF\theta4$). In addition, there was strong solar radiation in the diurnal cycle of pre-heatwave and heatwave periods, leading to the noticeable amplitude of $IMF\theta5$. Whereas, $IMFW1$, $IMFW2$ and $IMFW4$ tend to possess a larger amplitude during the non-heatwave ($IMFW1$: 0.84 m sec^{-1}, $IMFW2$: 1.07 m sec^{-1}, $IMFW4$: 0.35 m sec^{-1}) and the early pre-heatwave ($IMFW1$: 0.61 m sec^{-1}, $IMFW2$:

0.51 m sec^{-1}, *IMFW*4: 0.97 m sec^{-1}) periods.

The southwesterly monsoon in the non-heatwave and early pre-heatwave periods accompanied windy conditions [30]. Subsequently, the faster background winds enhanced the turbulence in street canyons (*IMFW*1), uphill/downhill flows (*IMFW*2), and urban-rural advection (*IMFW*4). On the other hand, *IMFW*1 to *IMFW*4 during the heatwave period are attributed to the secondary circulation induced by buoyancy rather than background winds. Besides, the IMF frequencies in the local-scale windows (IMF1 to IMF4) were compared for various periods. The temperature IMFs ($IMF\theta1$ to $IMF\theta4$) exhibit noticeable blue-shift (higher frequency) during the heatwave period ($IMF\theta1$: 0.051 cycles hr^{-1}, $IMF\theta2$: 0.097 cycles hr^{-1}, $IMF\theta3$: 0.220 cycles hr^{-1}, $IMF\theta4$: 0.394 cycles hr^{-1}) compared with the non-heatwave ($IMF\theta1$: 0.032 cycles hr^{-1}, $IMF\theta2$: 0.065 cycles hr^{-1}, $IMF\theta3$: 0.174 cycles hr^{-1}, $IMF\theta4$: 0.315 cycles hr^{-1}), pre-heatwave ($IMF\theta1$: 0.037 cycles hr^{-1}, $IMF\theta2$: 0.090 cycles hr^{-1}, $IMF\theta3$: 0.180 cycles hr^{-1}, $IMF\theta4$: 0.393 cycles hr^{-1}), and post-heatwave ($IMF\theta1$: 0.045 cycles hr^{-1}, $IMF\theta2$: 0.091 cycles hr^{-1}, $IMF\theta3$: 0.182 cycles hr^{-1}, $IMF\theta4$: 0.318 cycles hr^{-1}) ones. It is caused by the intensification of heat exchange and convection during the heatwave period.

However, the frequency of wind-speed IMFs during non-heatwave period (*IMFW*1: 0.043 cycles hr^{-1}, *IMFW*2: 0.098 cycles hr^{-1}, *IMFW*3: 0.239 cycles hr^{-1}, *IMFW*4: 0.348 cycles hr^{-1}) was enhanced by the (stronger) synoptic winds that tended to be higher than its pre-heatwave (*IMFW*1: 0.042 cycles hr^{-1}, *IMFW*2: 0.074 cycles hr^{-1}, *IMFW*3: 0.128 cycles hr^{-1}, *IMFW*4: 0.404 cycles hr^{-1}), heatwave (*IMFW*1: 0.021 cycles hr^{-1}, *IMFW*2: 0.081 cycles hr^{-1}, *IMFW*3: 0.174 cycles hr^{-1}, *IMFW*4: 0.432 cycles hr^{-1}), and post-heatwave (*IMFW*1: 0.0454 cycles hr^{-1}, *IMFW*2: 0.909 cycles hr^{-1}, *IMFW*3: 0.136 cycles hr^{-1}, *IMFW*4: 0.341 cycles hr^{-1}) counterpart. It is noteworthy that both the amplitude and frequency of temperature synoptic component (*IMFθ*6, blue block) dropped at the end of the heatwave period (Figure 15). It is because the formation of low-pressure system resulted in cooling and precipitation. Moreover, there was a reduction in the amplitude and frequency of wind-speed synoptic component (*IMFW*6) in the non-heatwave period that touched down in the early heatwave (June 23, 2016) period. It is mainly attributed to the development of subtropical ridge that resulted in stuff air and calm wind which are critical to the development of a heatwave event. Afterward, the frequency of *IMFW*6 gradually increased until the end of the heatwave period when the high-pressure system slowly declined to low-pressure.

Alike our findings, the strengthening of secondary circulation, such as land-sea breeze [60], heat storage [61] and anthropogenic heat [31], as well as the weakening of urban-rural advection [61] during heatwave events have been reported elsewhere. In addition, our current results detailed the variation of amplitude and frequency that provide insight of urban climate during heatwave events, effectuating mitigation strategies.

UHI is also aggravated during the heatwave period. It is found that urban areas are more sensitive to heatwave than rural areas. Unlike non-heatwave and pre-heatwave periods, the differences in urban-rural temperatures are more noticeable during the heatwave and post-heatwave periods (Figure 14). Hence, there exists synergy between heatwave and UHI that is in line with previous studies [61]. Moreover, our findings reveal the interaction between heatwave and UHI using NA-MEMD. Firstly, the hot ambient temperature during heatwave period enhances the heat storage, increasing urban-rural contrast in surface temperatures. It changes the amplitude of $IMF\theta1$, causing hotter peaked temperature. Secondly, heatwave intensifies the difference in urban-rural anthropogenic heat exhaust from air-conditioning systems that in turn raises the amplitude of $IMF\theta4$. Finally, weakened background winds also suppress the advective cooling induced by urban-rural air motions.

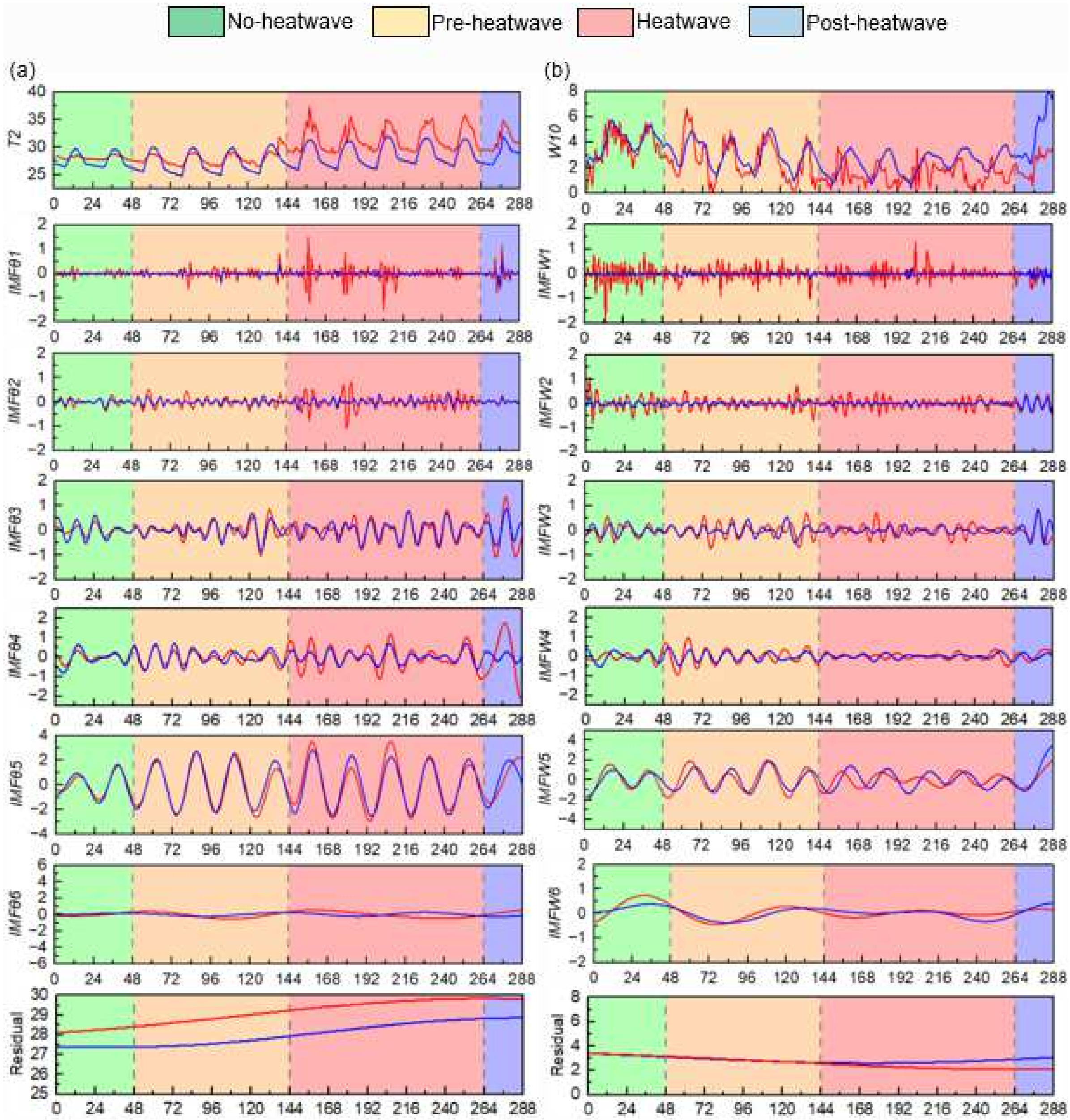

Figure 14. Time series of the original signals as well as the IMFs of (a) 2-m temperature *IMFθj* and (b) 10-m wind speed *IMFWj* during the non-heatwave (June 17 to 18, 2016), pre-heatwave (June 19 to 22, 2016), heatwave (June 23 to 27, 2016), and post-heatwave (June 28, 2016) periods after NA-MEMD for urban and rural areas.

521

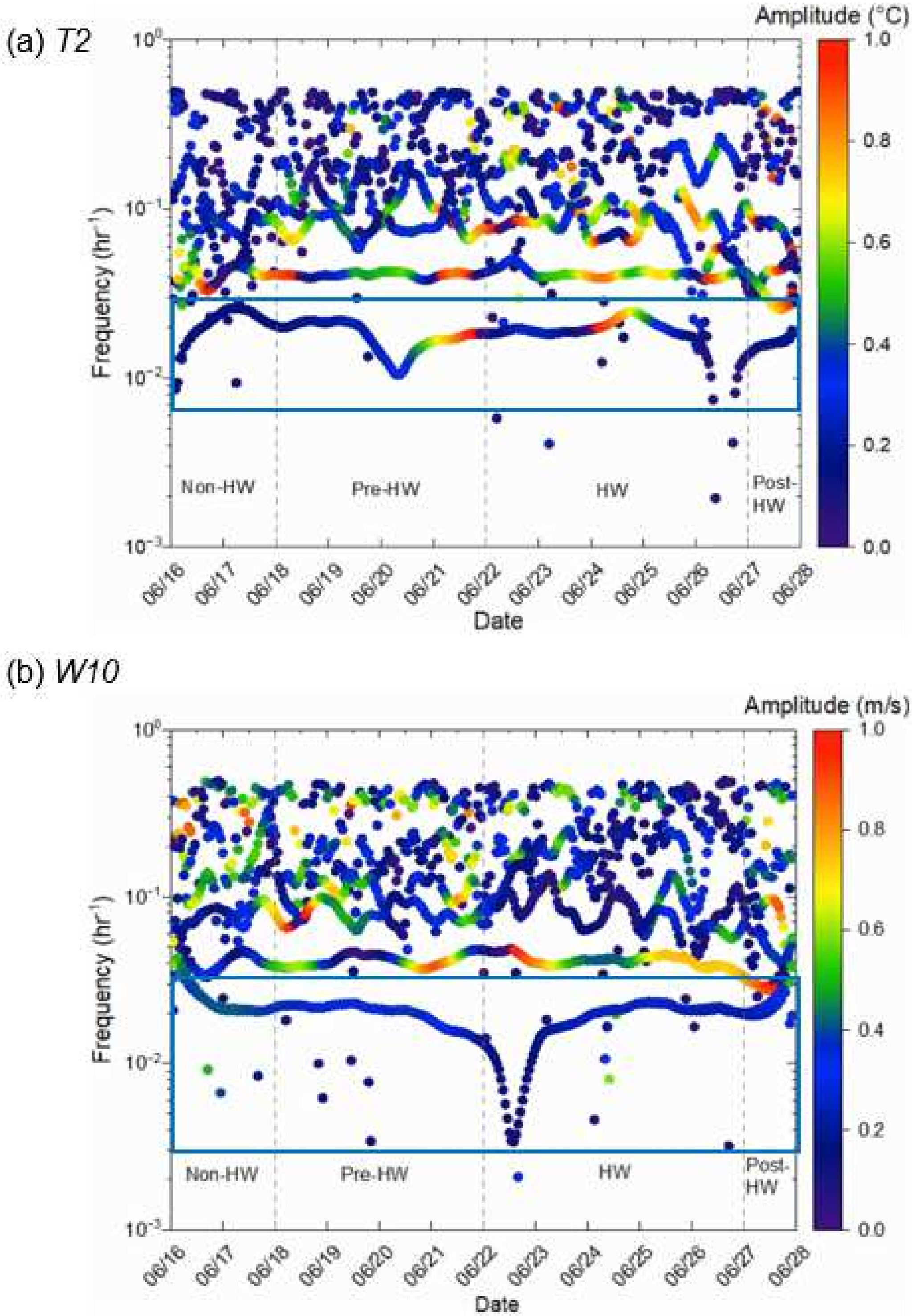

Figure 15. Comparison of Hilbert-Huang transform (HHT) spectra of (a) 2-m temperature *T*2 and (b) 10-m wind speed *W*10 during the non-heatwave (June 17 to 18, 2016), pre-heatwave (June 19 to 22, 2016), heatwave (June 23 to 27, 2016), and post-heatwave (June 28, 2016) periods in urban areas.

4. Conclusions

In this study, the meteorology parameters during a heatwave event in HK (June 23 to 28, 2016) are calculated using the multi-layer WRF-BEP/BEM model. The time series of urban temperature and wind speed from the WRF results are decomposed into various components in the time-frequency domain using HHT. After EMD, the physical explanation of each IMF of temperature and wind speed is explored by a series of numerical experiments. Furthermore, the effective range of high-frequency temperature fluctuations and the related susceptible urban areas are assessed through the peaked amplitude of IMFs. The key findings are summarized as follows:

1. The trend of 2-m temperature $T2$ and 10-m wind speed $W10$ during extremely hot days in urban areas could be partitioned into 6 IMFs. Among others, IMF6 is the low-frequency synoptic scale while IMF5 belongs to the periodic, diurnal-cycle window. IMF1 to IMF4 are grouped into local-scale windows which are aperiodic, high-frequency components. Under this circumstance, they are more likely to induce acute threat to power infrastructure. The temporal scales of IMF1, IMF2, IMF3, and IMF4 in temperature (wind speed) are 2.63 hr (2.53 hr), 5.88 hr (5.78 hr), 13.16 hr (9.84 hr), and 22.72 hr (19.05 hr), respectively. Accordingly, their spatial scales are 2.31 km (0.99 km), 4.29 km (1.65 km), 5.94 km (2.64 km), and 6.6 km (2.97 km).

2. The physical mechanism of IMF1 to IMF4 is elaborated as well. The temperature/wind-speed variations in the IMF1 component could be attributed to the disturbance caused by

the turbulent transport in street canyons and/or the heat-storage/release properties of building materials. The fluctuation in IMF2 is induced by the uphill/downhill flows in mountainous terrain. The land/sea breeze modifies the urban thermal context in the IMF3 components. The temperature and wind-speed fluctuations in the IMF4 components are attributed to the anthropogenic heat in urban and suburban areas.

3. The peaked amplitudes of temperature $IMF\theta 1$ to $IMF\theta 4$ cause the inhomogeneous, heat-related impact in cities. The effect of the IMF1 components is substantial in urban (1.4 °C $\leq IMF\theta 1 \leq$ 1.6 °C) but less significant (0.6 °C $\leq IMF\theta 1 \leq$ 1.0 °C) in rural areas. It is most appealing in compact high-rise (LCZ1) and open high-rise (LCZ4) areas where the ARs are high (2.75 $\leq$ AR $\leq$ 6). IMF2 (1 °C $\leq IMF\theta 2 \leq$ 2.1 °C) is most risky in foothill areas with an effective range of about 8 km. The littoral areas within 10 km from coastline are susceptible to IMF3 (0.6 °C $\leq IMF\theta 3 \leq$ 3.6 °C). IMF4 (2.5 °C $\leq IMF\theta 4 \leq$ 3.5 °C) tends to fluctuate most in urban and suburban areas where the anthropogenic heat is intense.

4. There exists a synergistic interaction between heatwave and UHI. Heatwave intensifies urban-rural temperature difference mainly by: (1) enhancing heat storage in construction material, (2) increasing anthropogenic heat, and (3) weakening the cool air motions from surrounding rural areas. On the other hand, the strengthening of land-sea secondary circulation is found during heatwave events.

Overall, to the best knowledge of the authors, this paper unprecedentedly characterizes multi-frequency components of air temperature and wind speed during a heatwave event together with unveil the physical mechanism behind. It could provide references for urban planners and policy makers, effectuating cost-effective strategies for public health as well as power security in a timely manner. Besides, the outcome provides an insight into the physical processes of urban temperature variation which are necessary when extreme heatwave events become more frequent in the current era under global warming.

The WRF setup used in this study was developed based on the Fortran W2W tool and WRF 3.6.1 [62, 63] that are commonly used in WRF modeling [64]. Whereas, the latest version of W2W tool [65] based on Python assigns morphological parameters directly to the higher-resolution LCZ map which is then aggregated to the lower-resolution WRF grids. It is able to capture urban diversity as well as reduces the uncertainty in urban-canopy parameters. Besides, the BEP/BEM model was updated in the new version of WRF to lower down memory consumption. Further efforts are worthy to modify the Python W2W tool and WRF 4.3 (or later), integrating the LCZBC data (30 urban classes).

Acknowledgments

This research is conducted in part using the research computing facilities and/or advisory services offered by Information Technology Services (ITS), The University of Hong Kong (HKU). Technical support from Ms. Lilian Y.L. Chan, Mr. W.K. Kwan, and Mr. Bill H.T. Yau is appreciated. This study is partly supported by the Hong Kong (HK) Research Grants Council (RGC) Theme-based Research Scheme (TRS)T24-504/17-N, the RGC

Collaborative Research Fund (CRF) C7064-18G, RGC CRF C5108-20G as well as the RGC General Research Fund (GRF) 17209819 and 17211322.

References

[1] A. Baniassadi, J. Heusinger, D.J. Sailor, Energy efficiency vs resiliency to extreme heat and power outages: The role of evolving building energy codes, Building and Environment, 139 (2018) 86-94.

[2] The Future of Cooling in China, Delivering on action plans for sustainable air conditioning, (2019).

[3] The Future of Cooling, Opportunities for energy- efficient air conditioning, (2018).

[4] B. Stone Jr, E. Mallen, M. Rajput, C.J. Gronlund, A.M. Broadbent, E.S. Krayenhoff, G. Augenbroe, M.S. O'Neill, M. Georgescu, Compound Climate and Infrastructure Events: How Electrical Grid Failure Alters Heat Wave Risk, Environmental Science & Technology, 55 (10) (2021) 6957-6964.

[5] C. Shen, W. Zhu, L. Xu, Critical risk determination method of energy-flow network for urban electricity system under extreme heat wave impact, Environmental Research, 191 (2020) 110143.

[6] W.B. Goggins, E.Y. Chan, E. Ng, C. Ren, L. Chen, Effect modification of the association between short-term meteorological factors and mortality by urban heat islands in Hong Kong, PloS one, 7 (6) (2012) e38551.

[7] W. Fung, K.S. Lam, W. Hung, S. Pang, Y. Lee, Impact of urban temperature on energy consumption of Hong Kong, Energy, 31 (14) (2006) 2623-2637.

[8] A. Christen, F. Meier, D. Scherer, High-frequency fluctuations of surface temperatures in an urban environment, Theoretical and Applied Climatology, 108 (2012) 301-324.

[9] D. Burillo, M.V. Chester, B. Ruddell, N. Johnson, Electricity demand planning forecasts should consider climate non-stationarity to maintain reserve margins during heat waves, Applied Energy, 206 (2017) 267-277.

[10] Y. Wang, Y. Li, Y. Xue, A. Martilli, J. Shen, P.W. Chan, City-scale morphological influence on diurnal urban air temperature, Building and Environment, 169 (2020) 106527.

[11] G. Chen, C.K.C. Lam, K. Wang, B. Wang, J. Hang, Q. Wang, X. Wang, Effects of urban geometry on thermal environment in 2D street canyons: A scaled experimental study, Building and Environment, 198 (2021) 107916.

[12] P. Pišoft, J. Kalvová, R. Brázdil, Cycles and trends in the Czech temperature series using wavelet transforms, International Journal of Climatology: A Journal of the Royal Meteorological Society, 24 (13) (2004) 1661-1670.

[13] Z. Wu, N.E. Huang, S.R. Long, C.-K. Peng, On the trend, detrending, and variability of nonlinear and nonstationary time series, Proceedings of the National Academy of Sciences, 104 (38) (2007) 14889-14894.

[14] N.E. Huang, Z. Shen, S.R. Long, M.C. Wu, H.H. Shih, Q. Zheng, N.-C. Yen, C.C. Tung, H.H. Liu, The empirical mode decomposition and the Hilbert spectrum for nonlinear and non-stationary time series analysis, Proceedings of the Royal Society of London. Series A: mathematical, physical and engineering sciences, 454 (1971) (1998) 903-995.

[15] V. Capparelli, C. Franzke, A. Vecchio, M.P. Freeman, N.W. Watkins, V. Carbone, A

spatiotemporal analysis of US station temperature trends over the last century, Journal of Geophysical Research: Atmospheres, 118 (14) (2013) 7427-7434.

[16] M.G. Orozco-del-Castillo, J.J. Hernández-Gómez, G.A. Yañez-Casas, M.R. Moreno-Sabido, C. Couder-Castañeda, I. Medina, R. Novelo-Cruz, M.A. Enciso-Aguilar, Pattern recognition through empirical mode decomposition for temperature time series between 1986 and 2019 in Mexico City downtown for global warming assessment, in: Telematics and Computing: 8th International Congress, WITCOM 2019, Merida, Mexico, November 4–8, 2019, Proceedings 8, Springer, 2019, pp. 45-60.

[17] W. Chu, S. Qiu, J. Xu, Temperature change of Shanghai and its response to global warming and urbanization, Atmosphere, 7 (9) (2016) 114.

[18] C. Yang, H. Wu, Y. Zhang, M. Itoh, Extracting periodic components in temperature fluctuation patterns, in: 2009 First International Conference on Information Science and Engineering, IEEE, 2009, pp. 4873-4876.

[19] M.-L. Lin, C.W. Tsai, C.-K. Chen, Daily maximum temperature forecasting in changing climate using a hybrid of Multi-dimensional Complementary Ensemble Empirical Mode Decomposition and Radial Basis Function Neural Network, Journal of Hydrology: Regional Studies, 38 (2021) 100923.

[20] A. Vecchio, V. Carbone, Amplitude-frequency fluctuations of the seasonal cycle, temperature anomalies, and long-range persistence of climate records, Physical Review E, 82 (6) (2010) 066101.

[21] S. Adarsh, M.J. Reddy, Investigating the multiscale variability and teleconnections of extreme temperature over Southern India using the Hilbert–Huang transform, Modeling

Earth Systems and Environment, 3 (2017) 1-17.

[22] M.M. Dedović, N. Dautbašić, S. Avdaković, Impact of air temperature on active and reactive power consumption-Sarajevo case study, B&H Electrical. Engineering, 11 (2017) 61-70.

[23] Z. Wen, S. Wu, J. Chen, M. Lü, NDVI indicated long-term interannual changes in vegetation activities and their responses to climatic and anthropogenic factors in the Three Gorges Reservoir Region, China, Science of the Total Environment, 574 (2017) 947-959.

[24] J. Zou, Y. Yu, J. Liu, J. Niu, K. Chauhan, C. Lei, Field measurement of the urban pedestrian level wind turbulence, Building and Environment, 194 (2021) 107713.

[25] F. Salamanca, A. Krpo, A. Martilli, A. Clappier, A new building energy model coupled with an urban canopy parameterization for urban climate simulations—part I. formulation, verification, and sensitivity analysis of the model, Theoretical and applied climatology, 99 (3) (2010) 331-344.

[26] F. Salamanca, A. Martilli, A new building energy model coupled with an urban canopy parameterization for urban climate simulations—Part II. Validation with one dimension off-line simulations, Theoretical and Applied Climatology, 99 (3) (2010) 345-356.

[27] J. Kong, Y. Zhao, J. Carmeliet, C. Lei, Urban heat island and its interaction with heatwaves: A review of studies on mesoscale, Sustainability, 13 (19) (2021) 10923.

[28] Y. Wang, Y. Li, S.D. Sabatino, A. Martilli, P. Chan, Effects of anthropogenic heat due to air-conditioning systems on an extreme high temperature event in Hong Kong, Environmental Research Letters, 13 (3) (2018) 034015.

[29] L.G.R. Santos, V.K. Singh, M.O. Mughal, I. Nevat, L.K. Norford, J.A. Fonseca, Estimating building's anthropogenic heat: a joint local climate zone and land use classification method, in: eSIM Conference 2021, 2020.

[30] HKO, The Weather of June 2016 https://www.hko.gov.hk/en/wxinfo/pastwx/mws2016/mws201606.htm, (2016).

[31] Y. Wang, Y. Li, S. Di Sabatino, A. Martilli, P. Chan, Effects of anthropogenic heat due to air-conditioning systems on an extreme high temperature event in Hong Kong, Environmental Research Letters, 13 (3) (2018) 034015.

[32] R. Wang, C. Ren, Y. Xu, K.K.-L. Lau, Y. Shi, Mapping the local climate zones of urban areas by GIS-based and WUDAPT methods: A case study of Hong Kong, Urban Climate, 24 (2018) 567-576.

[33] HKPlanD, Land Utilization Map, in: Planning Department, HKSAR (Ed.), (2018).

[34] P. Bougeault, P. Lacarrere, Parameterization of orography-induced turbulence in a mesobeta--scale model, Monthly weather review, 117 (8) (1989) 1872-1890.

[35] S.-Y. Hong, J. Dudhia, S.-H. Chen, A revised approach to ice microphysical processes for the bulk parameterization of clouds and precipitation, Monthly weather review, 132 (1) (2004) 103-120.

[36] F. Chen, J. Dudhia, Coupling an advanced land surface–hydrology model with the Penn State–NCAR MM5 modeling system. Part I: Model implementation and sensitivity, Monthly weather review, 129 (4) (2001) 569-585.

[37] J.S. Kain, J.M. Fritsch, A one-dimensional entraining/detraining plume model and its application in convective parameterization, Journal of Atmospheric Sciences, 47 (23)

(1990) 2784-2802.

[38] J. Dudhia, Numerical study of convection observed during the winter monsoon experiment using a mesoscale two-dimensional model, Journal of Atmospheric Sciences, 46 (20) (1989) 3077-3107.

[39] E.J. Mlawer, S.J. Taubman, P.D. Brown, M.J. Iacono, S.A. Clough, Radiative transfer for inhomogeneous atmospheres: RRTM, a validated correlated-k model for the longwave, Journal of Geophysical Research: Atmospheres, 102 (D14) (1997) 16663-16682.

[40] R. Du, C.-H. Liu, X.-X. Li, C.-Y. Lin, Effect of local climate zone (LCZ) and building category (BC) classification on the simulation of urban climate and air-conditioning load in Hong Kong, Energy, 271 (2023) 127004.

[41] N. ur Rehman, C. Park, N.E. Huang, D.P. Mandic, EMD via MEMD: multivariate noise-aided computation of standard EMD, Advances in adaptive data analysis, 5 (02) (2013) 1350007.

[42] HKPlanD, Urban climatic map and standards for wind environment - Feasibility Study. (2012).

[43] Y.Y. Yan, Surface wind characteristics and variability in Hong Kong, Weather, 62 (11) (2007) 312-316.

[44] H. Liu, J.C. Chan, An investigation of air-pollutant patterns under sea–land breezes during a severe air-pollution episode in Hong Kong, Atmospheric Environment, 36 (4) (2002) 591-601.

[45] H. Liu, J.C. Chan, Boundary layer dynamics associated with a severe air-pollution episode in Hong Kong, Atmospheric Environment, 36 (12) (2002) 2013-2025.

[46] M.-K. Hwang, J.-H. Bang, S. Kim, Y.-K. Kim, I. Oh, Estimation of thermal comfort felt by human exposed to extreme heat wave in a complex urban area using a WRF-MENEX model, International journal of biometeorology, 63 (7) (2019) 927-938.

[47] Y. Wang, S. Di Sabatino, A. Martilli, Y. Li, M. Wong, E. Gutiérrez, P. Chan, Impact of land surface heterogeneity on urban heat island circulation and sea-land breeze circulation in Hong Kong, Journal of Geophysical Research: Atmospheres, 122 (8) (2017) 4332-4352.

[48] Q. Wang, C. Zhang, C. Ren, J. Hang, Y. Li, Urban heat island circulations over the Beijing-Tianjin region under calm and fair conditions, Building and Environment, 180 (2020) 107063.

[49] U.S. EPA, Guidance on the use of models and other analyses for demonstrating attainment of air quality goals for ozone, PM2.5, and regional haze, in, United States Environment Protection Agency, Research Triangle Park, NC, 2007.

[50] European Environment Agency, The application of models under the European Union's Air Quality Directive: A technical reference guide, Copenhagen, 2011.

[51] C. Misenis, J. Thurman, R.C. Owen, Prognostic meteorological data in dispersion applications, in: Proceedings of the 19th International Conference on Harmonisation within Atmospheric Dispersion Modelling for Regulatory Purposes, Bruges, Belgium, 2019, pp. 3-6.

[52] D. Oettl, G. Veratti, A comparative study of mesoscale flow-field modelling in an Eastern Alpine region using WRF and GRAMM-SCI, Atmospheric Research, 249 (2021) 105288.

[53] HKO, Information of Weather Station, (2022) https://www.hko.gov.hk/en/cis/stn.htm.

[54] L.W. Siu, M.A. Hart, Quantifying urban heat island intensity in Hong Kong SAR, China, Environmental monitoring and assessment, 185 (5) (2013) 4383-4398.

[55] C. Helmis, G. Sgouros, H. Flocas, K. Schäfer, C. Jahn, M. Hoffmann, C. Heyder, R. Kurtenbach, A. Niedojadlo, P. Wiesen, The role of meteorology on the background air quality at the Athens International Airport, Atmospheric environment, 45 (31) (2011) 5561-5571.

[56] J. Barlow, G. Rooney, S. von Hünerbein, S. Bradley, Relating urban surface-layer structure to upwind terrain for the Salford Experiment (Salfex), Boundary-layer meteorology, 127 (2008) 173-191.

[57] H. Swaid, M.E. Hoffman, Prediction of urban air temperature variations using the analytical CTTC model, Energy and Buildings, 14 (4) (1990) 313-324.

[58] N.S.M. Harmay, M. Choi, Effects of heat waves on urban warming across different urban morphologies and climate zones, Building and Environment, 209 (2022) 108677.

[59] F. Guo, J. Zhao, H. Zhang, J. Dong, P. Zhu, S.S.Y. Lau, Effects of urban form on sea cooling capacity under the heatwave, Sustainable Cities and Society, 88 (2023) 104271.

[60] J. Hidalgo, V. Masson, L. Gimeno, Scaling the daytime urban heat island and urban-breeze circulation, Journal of Applied Meteorology and Climatology, 49 (5) (2010) 889-901.

[61] D. Li, E. Bou-Zeid, Synergistic interactions between urban heat islands and heat waves: The impact in cities is larger than the sum of its parts, Journal of applied Meteorology and Climatology, 52 (9) (2013) 2051-2064.

[62] O. Brousse, A. Martilli, M. Foley, G. Mills, B. Bechtel, WUDAPT, an efficient land use

producing data tool for mesoscale models? Integration of urban LCZ in WRF over Madrid. Urban Climate, 17 (2016) 116-134.

[63] A. Martilli, O. Brousse, J. Ching, Urbanized WRF modeling using WUDAPT. Paper presented at the Technical Report March, Cientro de Investigaciones Energeticas MedioAmbientales y Tecnologicas (CIEMAT), (2016).

[64] P. Patel, S. Jamshidi, R. Nadimpalli, D.G. Aliaga, G. Mills, F. Chen, M. Demuzere, D. Niyogi, Modeling Large-Scale Heatwave by Incorporating Enhanced Urban Representation. Journal of Geophysical Research: Atmospheres, 127(2) (2022) e2021JD035316.

[65] M. Demuzere, D. Argüeso, A. Zonato, J. Kittner, W2W: A Python package that injects WUDAPT's Local Climate Zone information in WRF. Journal of Open Source Software, 7(76) (2022) 4432.